Petroleum Science 23 (2026) 4165–4182

Contents lists available at ScienceDirect

Petroleum Science

journal homepage: www.keaipublishing.com/en/journals/petroleum-science

Original Paper

Research on low-viscosity high-elastic fracturing fluid system with specific recognition and supramolecular assembly

Hao Bai [a], Fu-Jian Zhou [a,*], Zhi-Yuan Ding [a], Xin-Lei Liu [a], Sai Zhang [a], Kun Zhang [a], Wen-Jie Xie [a], Yun-Jin Wang [a], Rui-Jie Fei [a], Yue-Peng Dong [b], Er-Dong Yao [a,**]

[a] State Key Laboratory of Petroleum Resources and Engineering, China University of Petroleum (Beijing), Beijing, 102249, China
[b] Liaoning Normal University, Dalian, 116029, Liaoning, China

ARTICLE INFO

Article history:
Received 9 October 2025
Received in revised form
13 March 2026
Accepted 14 March 2026
Available online 17 March 2026

Edited by Yan-Hua Sun

Keywords:
Electrostatic interaction
Hydrophobic association
Dynamic/static sand carrying
Viscoelastic properties

ABSTRACT

Fracturing fluids for tight sandstone reservoirs often suffer from issues such as low sand-carrying efficiency, difficulties in fracturing and gel breaking caused by high viscosity, and increased costs in practical applications. Therefore, there is an urgent need to develop a high-performance friction reducer system that combines both low viscosity and high elasticity. In this study, a chemical reduced-friction system (CRS-10, a polymer) with specific recognition capability is synthesized via aqueous solution polymerization. The monomer molar ratio of acrylamide to acrylic acid to quaternary ammonium hydrophobic monomer is 86.5:12.5:1.0. Subsequently, through electrostatic assembly with anionic nanoemulsion, a stable supramolecular three-dimensional network structure is successfully constructed. This system exhibited notably low viscosity alongside high elasticity. At the same polymer concentration, the elastic modulus at zero shear rate of the CRS-10 fluid system increases by 9376.97 times after assembly, and at the same viscosity, its elastic modulus increases by 2570.19 times. Under high-temperature conditions (120 °C) and high shear rate (170 s^{-1}), the system's viscosity remains stable above 30 mPa·s, demonstrating excellent temperature and shear resistance. Sand-carrying performance tests show that CRS-10 fluid system can carry sand particles for up to 5 h under static conditions without significant settling, and its yield stress far exceeds the net gravity of the sand particles. In dynamic sand-carrying tests, the sand equilibrium bank height reaches only about 30% of the fracture height, indicating outstanding sand-carrying capacity. The system's friction reduction rate exceeds 70%, consistent with conventional friction reduction models. The gel-breaking fluid is clear and transparent, with residue content below 50 mg/L. Furthermore, tight sandstone imbibition tests conducted in the laboratory confirm a significant increase in oil recovery rate, reaching as high as 42.7%. Mechanistic analysis using nuclear magnetic resonance (NMR) and transmission electron microscopy (TEM) reveals that the strong electrostatic interaction between the quaternary ammonium cations and sulfonate anions drives the supramolecular assembly to form a three-dimensional network with a wall thickness of 17.96 μm, which provides a physical basis for the high elasticity of the CRS-10 fluid system. Conductivity tests show that the interaction between anions and cations leads to a turning point change in conductivity and a significant decrease in the surface tension as the polymer concentration increases. This verifies that the polymer promotes surfactant adsorption and enrichment at the interface, thereby stabilizing the supramolecular structure. This supports the correlation between the assembly mechanism and improved rheological properties. In summary, the CRS-10 fracturing fluid system based on specific recognition and supramolecular assembly effectively overcomes the limitations of weak sand-carrying capacity and high viscosity costs associated with traditional slickwater fluids, offering a novel slickwater system with promising applications for efficient fracturing of tight sandstone reservoirs.

1. Introduction

As the key fluid system for hydraulic fracturing in tight sandstone reservoirs, large-displacement friction reduction and ability of slickwater to create complex fractures decisively influence

* Corresponding author.
** Corresponding author.
E-mail addresses: zhoufj@cup.edu.cn (F.-J. Zhou), yaoed@cup.edu.cn (E.-D. Yao).
Peer review under the responsibility of China University of Petroleum (Beijing).

https://doi.org/10.1016/j.petsci.2026.03.032

fracturing effectiveness (Yang et al., 2019; Yang F. et al., 2024; Zhao et al., 2023). With increasing requirements on sand-carrying performance, high viscosity friction reducers (HVFRs) have rapidly developed due to their rheological advantages (Cai et al., 2023; Wang et al., 2022; Wang et al., 2024). Compared with conventional low-viscosity slickwater, HVFRs not only significantly improve the suspension stability and transport uniformity of sand particles by optimizing the viscoelasticity of fluid, but also effectively solve the problem of proppant carrying of conventional fluids in complex fracture networks (Liu et al., 2020; Shi et al., 2023; Wang et al., 2023). This advancement has significantly enhanced proppant placement efficiency and fracture conductivity of fracturing construction, making HVFRs a promising direction for tight sandstone stimulation. However, the mechanism of improving sand-carrying capacity by viscosity has clear limits (Zang et al., 2024; Zorgani et al., 2018). High-viscosity fluid increases pipeline friction and pumping energy, and can cause pressure fluctuations that destabilize operations (Jin et al., 2025; Wang et al., 2020). This fluid makes it difficult to achieve effective shear flow in the fracture, and it is impossible to form a complex fracture network structure. It is usually characterized by a large fracture width but a short length, that is, the reservoir stimulation volume (RSV) is small (Huang et al., 2024; Lei et al., 2022). Incomplete gel breaking leaves residues that may block micropores and irreversibly damage permeability, compromising long-term well productivity (Xu Z. et al., 2024; Zhang et al., 2022). Moreover, high polymer costs and required equipment/process upgrades raise operating expenses, limiting large-scale deployment in unconventional plays (Hincapie et al., 2022). Therefore, the development of a new fracturing fluid system with low viscosity and high sand-carrying capacity has become a key problem to be solved in the field of tight oil and gas stimulation technology.

Given the insufficient sand-carrying performance of HVFRs, researchers have optimized it by various means. These include developing new nanomaterial enhancers, using surfactants to adjust rheological properties, and employing smart responsive materials to dynamically control sand-carrying performance (Hu et al., 2024; Yao et al., 2021; Yehia et al., 2024). Examples include MoS_2-modified slickwater with improved rheology and sand carrying capacity (Xu H. et al., 2023a), silica nanoparticle-enhanced fluids that increased sand carrying capacity by 23% and broke rapidly with low damage (Liu et al., 2022), and zwitterionic VES blended with polymers to boost temperature resistance and tackifying effects while reducing chemical load (Othman et al., 2022). The pH-responsive low-friction polymer fracturing fluid developed by Bai et al. (2024) enhanced the hydration and crosslinking of the polymer by adjusting the pH, promoted the formation of a stable network, and improved the sand-carrying capacity in the low viscosity stage. Though effective to some extent, these approaches often suffer from limited enhancement, stability issues, high cost, or complexity that hinder industrial adoption. Recently, the elastic sand-carrying mechanism has emerged as a superior option (Bai et al., 2025; Zhao et al., 2021). Relying on its inherent elastic recovery force, low viscosity and high elastic fluid can not only effectively resist sand settlement and greatly improve sand-carrying efficiency, but also maintain low flow resistance, reduce pumping burden and gel breaking difficulty, thus reducing the potential damage to the reservoir (Han et al., 2024; Yang Z. et al., 2024). The core of elastic sand-carrying lies in the construction and response of the elastic network inside the fluid. When the fluid is subjected to shear force or external disturbance, the elastic network deforms and stores energy. When the shear force is weakened, the polymer network recovers rapidly, providing elastic restoring force to carry the sand particles, preventing gravity settlement and accumulation. This maintains uniform suspension and imparts elastic-like behavior to the fluid (Ma et al., 2024; Zarrin et al., 2024). In this way, the elastic sand-carrying mechanism realizes the perfect combination of low viscosity and high elasticity, and brings efficient sand-carrying effect.

Highly elastic liquids are commonly built by physical or chemical crosslinking or supramolecular self-assembly between polymer chains to form elastic 3D networks (Liu et al., 2025; Xu H. et al., 2024). The traditional mechanism of entropy elasticity is mainly derived from the recovery of elastic stretching of polymer chains, and the typical representative of which is the polymer gel systems such as polyacrylamide. Keane et al. (2024) and Gusev and Schwarz (2019) discussed the entropy elastic properties of these gels and their effects on rheological properties. However, the friction reduction performance of the fluid system synthesized by chemical crosslinking, such as gel fracturing fluid (guar), is generally poor. In recent years, supramolecular assembly technology has developed rapidly. Researchers have constructed dynamic and highly ordered three-dimensional network structures such as surfactants (VES) and hydrophobically associating polymers through non-covalent interactions such as electrostatic interactions, hydrogen bonds and van der Waals forces. This kind of network not only improves the elastic modulus and structural stability of the fluid but also maintains good fluidity and excellent sand-carrying performance while maintaining low viscosity (Mao et al., 2022; Mohammadi et al., 2024). For example, Wen et al. (2024) and Hu et al. (2023) reported supramolecular polymer network systems based on hydrogen bonding and electrostatic interactions, which significantly improved fluid performance. Nevertheless, their synthesis processes are complicated, and stability, temperature and shear resistance often need improvement. Most systems also lack the function of imbibition mobilization and oil displacement. Furthermore, traditional VES systems require high dosage, and the associative polymer usually requires a higher concentration, which restricts their practical application.

To overcome limitations of existing conventional assembly systems such as high additive dosage, poor thermal and shear stability, complex fabrication, and residual damage, a low-molecular-weight friction reducer CRS-10 containing a small fraction of cationic recognition monomer is designed and combined with an anionic nano-emulsion to induce specific electrostatic recognition and form a three-dimensional supramolecular network at low concentrations. After assembly, the fluid system exhibits low viscosity while elasticity is dramatically enhanced: The elastic modulus at 0.01 Hz is increased up to 9376.97 times, and for the same viscosity the elastic modulus is increased by approximately 2570 times. The assembled system maintains viscosity greater than 30 mPa·s at 120 °C under 170 s^{-1} shear, sustains static sand suspension for at least 5 h, produces transparent gel-breaking with residue below 50 mg/L, achieves friction reduction greater than 70%, and enhances tight-sandstone oil recovery to 42.7% in imbibition tests. Compared with prior high-dosage VES or associative polymer systems, the method achieves equivalent or superior elastic sand-carrying at much lower additive levels, shows improved temperature and shear resistance, simplifies processing and reduces cost, and provides additional oil-mobilization benefits via nano-emulsion wettability modification. These features indicate that the CRS-10 supramolecular slickwater

has strong potential for practical application in tight sandstone fracturing.

2. Experimental materials and methods

2.1. Synthesis, characterization, and analysis of experimental reagents

2.1.1. The synthesis method and molecular structure of CRS-10 friction reducer

The synthesis of CRS-10 friction reducer is carried out by aqueous solution polymerization. The specific methods are as follows.

(1) Acrylamide (AM), acrylic acid (AA), and quaternary ammonium cationic hydrophobic monomer (DMAAC18) are added to a wide-mouth bottle at a molar ratio of 86.5:12.5:1.0, and distilled water is used as a solvent to prepare a solution with a total monomer concentration of 25 wt%. Subsequently, to facilitate the narrative, wt% is abbreviated to %.
(2) The uniformly stirred solution is poured into a multi-necked flask and placed in a low-temperature water bath at 16 °C for 30 min. At the same time, the solution is sealed and deoxygenated with nitrogen.
(3) The initiator ammonium persulfate and sodium bisulfite are prepared into 0.2% solution in the dropper, respectively. The solution to be polymerized in the flask is stirred on the electromagnetic stirrer while adding the diluted initiator. The solution is slowly dripped through the syringe. After the solution has obvious viscosity, it is transferred to a 50 °C water bath for 6 h.
(4) The reaction mixture is transferred to a beaker and soaked in a large amount of ethanol. The reaction mixture is cut to the size of rice grains with scissors. Finally, the product is vacuum-dried to constant weight and ground to obtain the CRS-10 dry powder friction reducer. The molecular structure of the polymer is shown in Fig. 1, and its molecular weight M_w is found to be 127.7114 million by gel permeation chromatography (GPC) test method.

2.1.2. Synthesis and characterization of CRS-10 friction reducer polymer

The synthesized CRS-10 friction reducer polymer powder is detected by Fourier transform infrared spectroscopy (FTIR) and nuclear magnetic resonance hydrogen (^{1}H NMR) spectrum, respectively. The FTIR analysis in Fig. 2(a) shows that the broad peak at 3205.11 cm^{-1} corresponds to the N–H stretching vibration of the acrylamide (AM) amide group, reflecting the formation of an intermolecular hydrogen bond network. The absorption peak at 1563.99 cm^{-1} indicates that there is an interaction between the amide group and the acrylic acid (AA) carboxylate (–COO). The absorption peaks at 2856.06 and 1324.86 cm^{-1} indicate the characteristic structures of long-chain alkyl and quaternary ammonium cations of DMAAC18 monomer. No vinyl C=C vibration is detected in the range of 1620–1680 cm^{-1}, indicating that the double bonds of AM, AA, and DMAAC18 are fully involved in the copolymerization reaction, which verifies the integrity of the polymer structure and design expectations.

The ^{1}H NMR analysis in Fig. 2(b) further confirms the results of the infrared spectrum test. The broad peak of 6.00–6.07 ppm corresponds to the N–H protons on the AM amide group, reflecting intermolecular hydrogen bonds and dynamic assembly. The multiple peaks of 0.47, 0.64, and 1.00 ppm are attributed to the ortho-methyl and long-chain terminal methyl groups of DMAAC18, showing the de-shielding effect of quaternary ammonium cations and the spatial accumulation of alkyl groups. 1.60 ppm single peak corresponds to the main chain or long chain methylene proton. The lack of vinyl proton signal at 4.5–5.5 ppm indicates that the monomer double bond has been completely reacted. The carboxylic acid matrix peak at 12.5–13.5 ppm only appears in acidic conditions and disappears in the form of polymer sodium salt, which proves that AA is successfully incorporated into the main chain. The overall NMR spectrum peak is highly consistent with the designed structure of CRS-10, which proves the successful synthesis of the target polymer.

2.1.3. Nano-emulsions of different ionic types

As an efficient fracturing fluid additive, nano-emulsion has a stable nanostructure. It is composed of alcohols, oil cores, and surfactants, which can realize the sustained release of surfactant and prolong the interaction time. Moreover, it is easily soluble in crude oil, significantly reduces the interfacial tension, modifies the wettability of rock matrix, and significantly improves the oil mobilization effect. Therefore, in this study, nano-emulsions with different ion surfactant types (the same effective content of surfactant) are selected for screening after supramolecular assembly with CRS-10 friction reducer polymer. Among them, the nano-emulsions with anionic surfactant, including sodium dodecyl benzene sulfonate (SDBS), sodium fatty alcohol ether sulfate (AES), and α-olefin sulfonate (AOS-1). Nano-emulsions with nonionic surfactant as the main agent, including styrene phenol polyoxyethylene ether (AE600) and fatty alcohol polyoxyethylene ether (AEO). Nano-emulsions with cationic surfactant as the main agent include dodecyl trimethyl ammonium chloride (DTAC) and cetyl trimethyl ammonium bromide (CTAB).

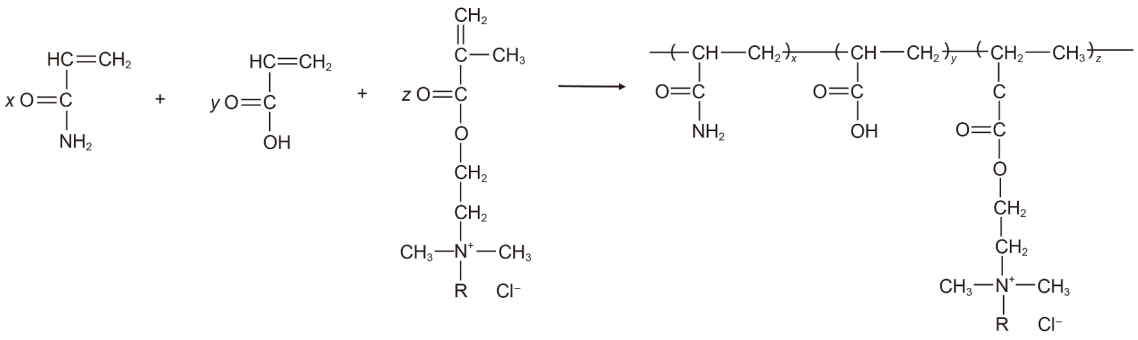

Fig. 1. Schematic diagram of molecular structure synthesis of CRS-10 friction reducer polymer.

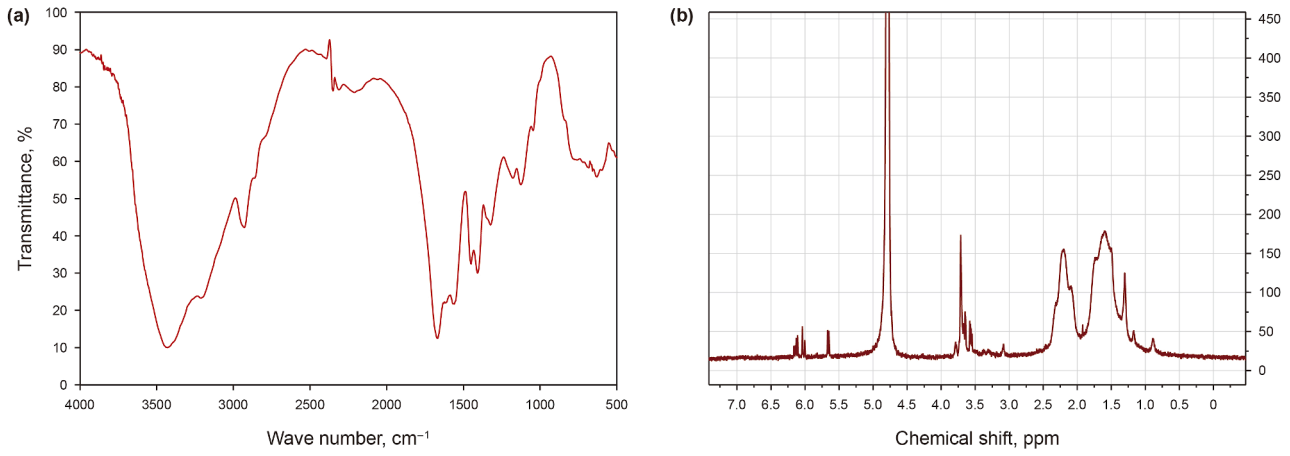

Fig. 2. FTIR (**a**) and ^{1}H NMR (**b**) spectra of CRS-10 friction reducer polymer.

2.2. Experimental method

2.2.1. Measurements of rheological properties

(1) Viscosity test

To simulate the field environment as much as possible, IKA mechanical stirrer is selected for fluid preparation in this study. Viscosity is one of the important indicators commonly used in the field to characterize the ability of fluid to carry proppant. Therefore, the use of a six-speed viscometer for laboratory measurement can not only quickly observe the viscosity changes before and after the assembly of the friction reducer polymer solution and the surfactant, but also realize the real-time adjustment of the fluid concentration. In this study, the shear rate of 170 s^{-1} (i.e., 100 RPM) is selected for testing, because the rate is close to the actual shear rate of the fluid in the wellbore, and it is often used as a reference standard for field evaluation of fluid sand transport capacity (Zhang et al., 2024; Xu H. et al., 2024).

(2) Temperature and shear resistance test

The assembled fluid system is placed in the HAKKE rheometer cavity for shear test. At the beginning, the sample is sheared at a constant shear rate, and at the same time, the temperature is increased at a rate of 3 °C/min until the simulated reservoir temperature is reached. After the temperature is stable, it continues to be maintained for 60 min at the same shear rate. The shear rates can be set as 5, 100, or 170 s^{-1}, which correspond to the fluid shear rates in the fracture, the transition zone from the fracture to the wellbore, and the wellbore, respectively (Zhang et al., 2024; Xu H. et al., 2024).

(3) Viscoelasticity test

Firstly, the HAKKE rheometer is used to scan the stress of the fluid sample, and the median of the stress stable interval is selected as the test stress (commonly 0.1 Pa). Subsequently, frequency scanning is performed under this stress, and the frequency range is set to 0.01 to 100 Hz. By analyzing the intersection of elastic modulus G'' and viscous modulus G' and the range of elastic interval, the viscoelastic properties of the solution after assembly are judged.

(4) Yield stress

The assembled fluid system is placed in the cavity of HAKKE rheometer to test the variable shear rate at room temperature. The shear rate range is set from 0.01 to 1000 s^{-1}, and the corresponding stress change curve is measured and recorded to obtain the yield stress value. Or, fixed shear frequency (commonly 1 Hz), variable shear stress test at room temperature, shear stress range is set to 0.01 to 20 Pa, the test can directly get the yield stress linear platform and threshold inflection point.

2.2.2. Sand-carrying capacity test

(1) Static sand settling test at different temperatures

The static sand settling experiment is carried out in a 100 mL measuring cylinder, and the sand concentration is set to 20%. Sand concentration (%) is defined as the ratio of proppant volume to fluid volume. The experimental steps are as follows: 100 mL of prepared fluid is added to the measuring cylinder, and the corresponding amount of 40/70 mesh quartz sand proppant is added. After mixing evenly, the settling time is recorded with a stopwatch.

To explore the influence of temperature on the fluid sand-carrying capacity, the above preferred concentration and type of sand-carrying fluid are placed in the oven, and the sand-carrying test is carried out at 70, 100, and 120 °C, respectively. Each temperature is maintained for 2 h to observe the settlement of proppant in the fluid. The test devices and suggestions at different

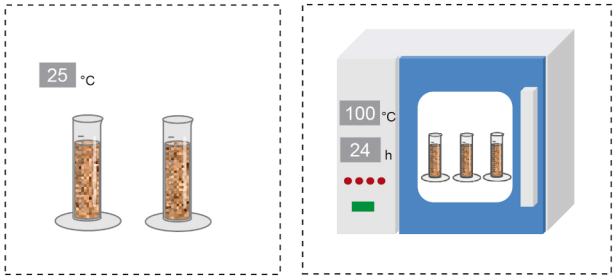

Fig. 3. Schematic diagram of static sand settling device at room temperature (25 °C) and reservoir temperature.

temperatures are shown in Fig. 3. Since the reservoir temperature usually exceeds the boiling point of the fluid, a stopper is installed above the measuring cylinder to prevent fluid evaporation.

(2) Fracture model dynamic sand-carrying method

For natural rock samples, they are first cut into cubes and subjected to triaxial fracturing to form a fracture surface. The fracture plate that can be closed is prepared by 3D printing and epoxy resin casting technology to simulate the shape and roughness of fractures. The fracture plate is installed on the steel frame, formed into a visual fracture model, and the fracture width is adjusted to about 0.60 cm. The sand conveying system is composed of a 40 L mixing tank and an adjustable frequency injection pump. The sand-carrying fluid is injected from the inlet of the fracture model, flows out after passing through the fracture and returns to the mixing tank to form a circulating flow. In the experiment, the sedimentation and accumulation of sand particles under different conditions were observed.

2.2.3. Friction reduction, gel breaking, and imbibition performance tests

(1) Friction-reduction testing

The device is mainly composed of an infusion system, a fracture simulation pipeline system, and a data acquisition and control system. The mixing tank is equipped with a stirring device for mixing and preparing fluid. The fluid is transported by the screw pump under the fluid distribution tank to ensure stable flow. The conveying fluid flows through a stainless steel wellbore simulation pipe (inner diameter 8 mm), and the pipe connection is equipped with a flow meter and a pressure difference meter for real-time monitoring of flow velocity and pressure difference. After the fluid flows through the test pipe, it flows back to the fluid distribution tank through the hose to form a cycle to ensure that the fluid is fully mixed and the measurement data is stable. By calculating the pressure difference ratio of different fluids (such as clear water and slickwater), the friction reduction performance is evaluated. The calculation formula is as follows:

$$R = \frac{\Delta P_O - \Delta P_{DR}}{\Delta P_O} \times 100\% \quad (1)$$

where R is the friction reduction rate, %; ΔP_O is the pressure drop of clear water, kPa; ΔP_{DR} is the pressure drop after adding the friction reducer, kPa.

(2) Gel-breaking and imbibition testing

A certain concentration of ammonium persulfate (400 mg/L) is added to the assembled fluid system, and different reservoir temperatures are simulated by water bath heating to perform gel breaking and residue testing. After the completion of gel breaking, the saturated oil core is immersed in the CRS-10 gel-breaking solution system to simulate the imbibition experiment of the soaking well under reservoir temperature.

3. Experimental results and analysis

3.1. Rheological properties

3.1.1. Formulation optimization of CRS-10 fluid system

The concentration of CRS-10 fluid is initially set to 0.20%. Critical overlap concentration (c^*) calculations and laboratory tests show chain overlap/assembly begins ≈0.08% (elasticity increases markedly above 0.075%), and 0.20% CRS-10 fluid fully carries sands while being the most cost-effective (Mahata and Mondal, 2024; Wang et al., 2019). The viscosity of the base fluid before assembly with the nano-emulsion is about 15 mPa·s. Compared with the non-ionic surfactant without charge, the ionic surfactant with charge, especially the anionic nano-emulsion, is more conducive to the effective assembly with the CRS-10 polymer solution to achieve a rapid increase in viscosity. Fig. 4(a) shows that the anionic nano-emulsion corresponds to a higher viscosity after assembly. Among them, the SDBS nano-emulsion with low concentration (0.05%) shows a more significant increase in viscosity after assembling with CRS-10, and the viscosity decreases slightly with the increase in the nano-emulsion concentration. The viscosity of the other two anionic nano-emulsions decreases significantly after increasing the concentration, indicating that the critical assembly concentration (CAC) is reached and the fluid system tends to be unstable.

As shown in Fig. 4(b), the addition of 0.10% SDBS nano-emulsion at a low polymer concentration has a surfactant self-assembly phenomenon (viscosity results show that the degree of change is small). With the increase in the concentration of friction reducer, its strength (viscosity) is still lower than 0.05% SDBS, indicating that the assembly effect of the two is reduced at this

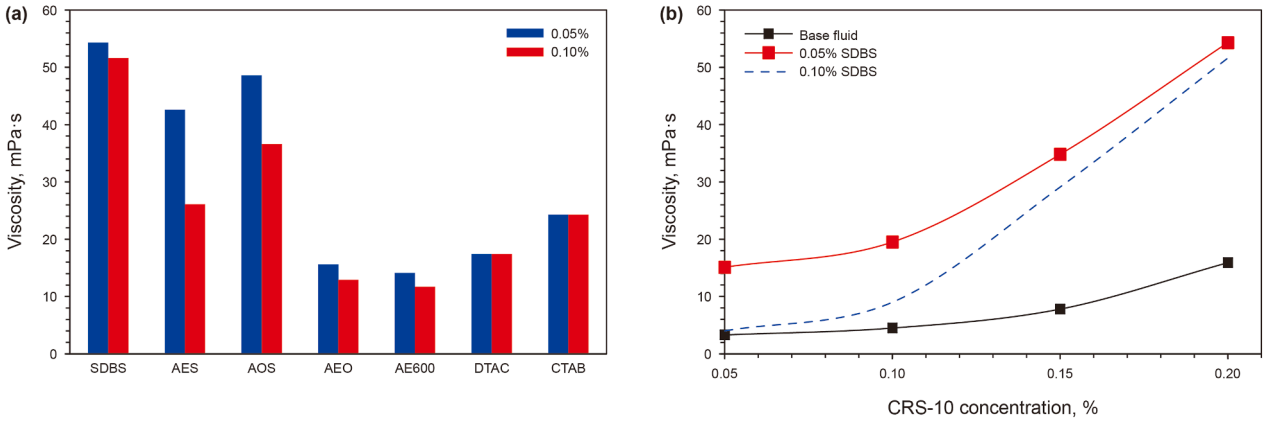

Fig. 4. Viscosity of nano-emulsions with different concentrations (types) after assembly with CRS-10. (**a**) Effect of nano-emulsion type and concentration; (**b**) effect of CRS-10 concentration.

time. Therefore, 0.05% anionic SDBS nano-emulsion is selected as the assembled fluid system. Subsequently, the concentration of SDBS nano-emulsion is fixed, and the amount of CRS-10 polymer is adjusted for assembly and viscosity measurement. The results show that the low concentration of CRS-10 polymer is difficult to assemble effectively, especially when its concentration is lower than that of nano-emulsion, the assembly effect is poor, indicating that more polymer is needed. With the increase in CRS-10 concentration, the viscosity after assembly increases significantly (increased by 3.42 times), and when the CRS-10 concentration reaches 0.20%, the viscosity stabilizes, suggesting that the assembly structure becomes stable (as shown by the red curve in Fig. 4(b)). Therefore, in the follow-up study, the concentration of CRS-10 can be selected at 0.05%–0.20%, and it can be used in conjunction with a fixed concentration of SDBS nano-emulsion (0.05%) to obtain an optimized viscosity-increasing effect through assembly.

3.1.2. Temperature resistance and shear resistance of CRS-10 fluid system

The rheological properties of the preferred SDBS nano-emulsion and CRS-10 polymer assembled system (0.20% CRS-10 + 0.05% SDBS) are tested at three temperatures of 70, 100, and 120 °C at different shear rates (170, 100, and 5 s^{-1}). The results show that the assembled fluid system exhibits excellent high temperature resistance and shear stability as shown in Fig. 5. Under the simulated wellbore shear condition of 170 s^{-1}, the viscosity of the system remains above 30 mPa·s after 1 h of shear, showing good structural stability. The viscosity is maintained at about 50 mPa·s at the shear rate of 100 s^{-1} during the simulation of the transition from wellbore to fracture, which ensures the flow performance and sand-carrying capacity. Under the condition of low shear rate of 5 s^{-1} (near zero shear), the viscosity increases significantly, exceeding 800 mPa·s, indicating that the fluid system has good sand-carrying performance in the fracture (as shown in Fig. 5(a–c)). Finally, to assess the durability of the three-dimensional architecture under realistic operational conditions, long-term shear tests at elevated temperature and high shear rate are performed. The results indicate that the CRS-10 system exhibits good durability and recoverability: Even after prolonged shearing its reversible network remains intact and the viscosity stays stable (as shown in Fig. 5(d)).

Few conventional VES fracturing fluids withstand temperatures ≥120 °C, and those that tolerate ~150 °C are extremely rare. Due to a polymer-reinforced 3D network scaffold, the CRS-10 assembled system shows clear advantages at high temperature, including improved thermal stability, shear resistance, and sand-carrying capability. Moreover, the CRS-10 fluid system requires only about 0.05%–0.20% polymer, compared with 3%–4% typically required for VES, offering a clear dosage and cost advantage (Liu et al., 2023; Xu H. et al., 2023; Zhang W. et al., 2020). In summary, the supramolecular assembly of CRS-10 and SDBS demonstrates excellent temperature and shear resistance, which helps meet proppant-carrying requirements in complex reservoir environments.

3.1.3. Viscoelastic properties before and after CRS-10 assembly

The viscoelastic modulus of the samples before and after the assembly of the preferred SDBS nano-emulsion with different concentrations of CRS-10 polymer is tested at different temperatures, and the shear frequency range is set to 0.01 to 10 Hz. The

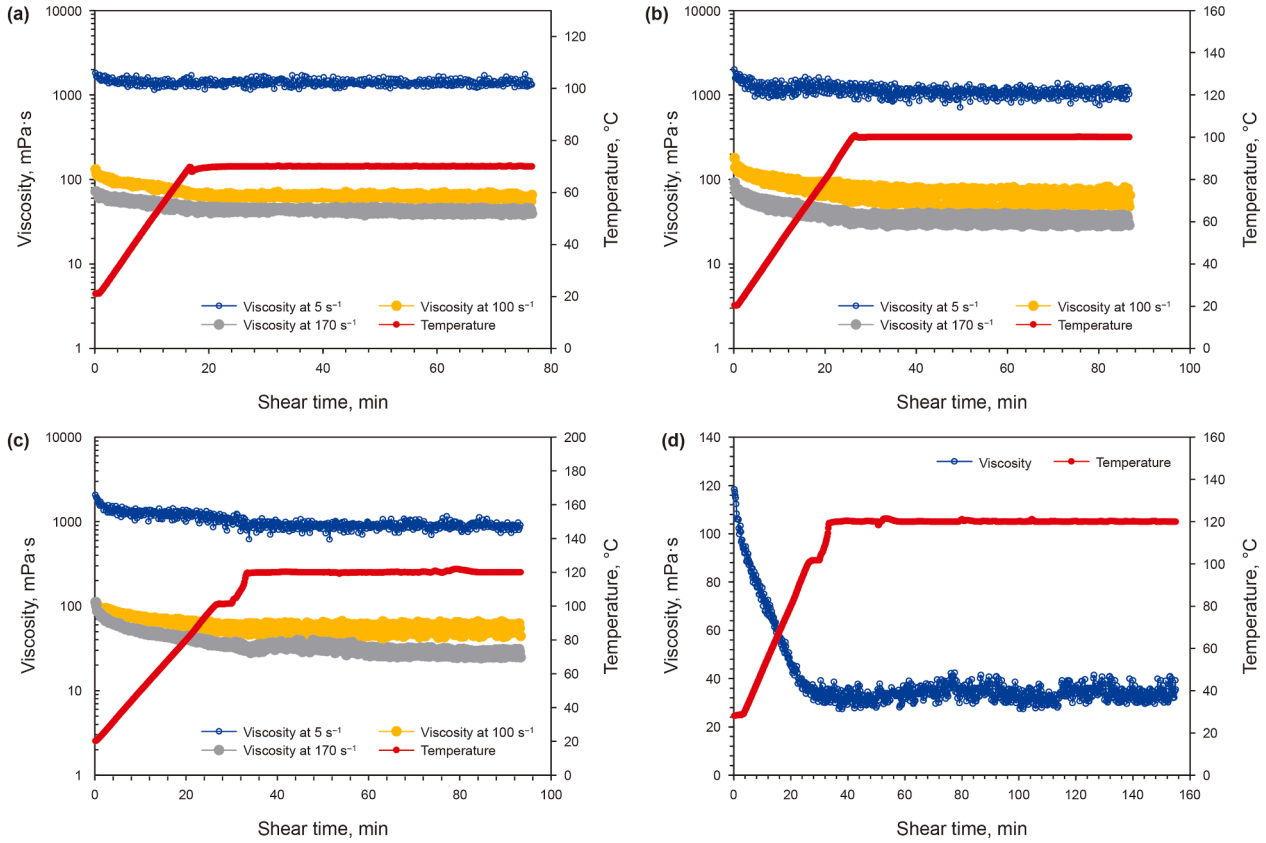

Fig. 5. Rheological properties of SDBS nano-emulsion and CRS-10 polymer assembled system at different shear rates and temperatures. (**a**) 70 °C; (**b**) 100 °C; (**c**) 120 °C; (**d**) 170 s^{-1}, 120 °C, prolonged shearing of 2 h.

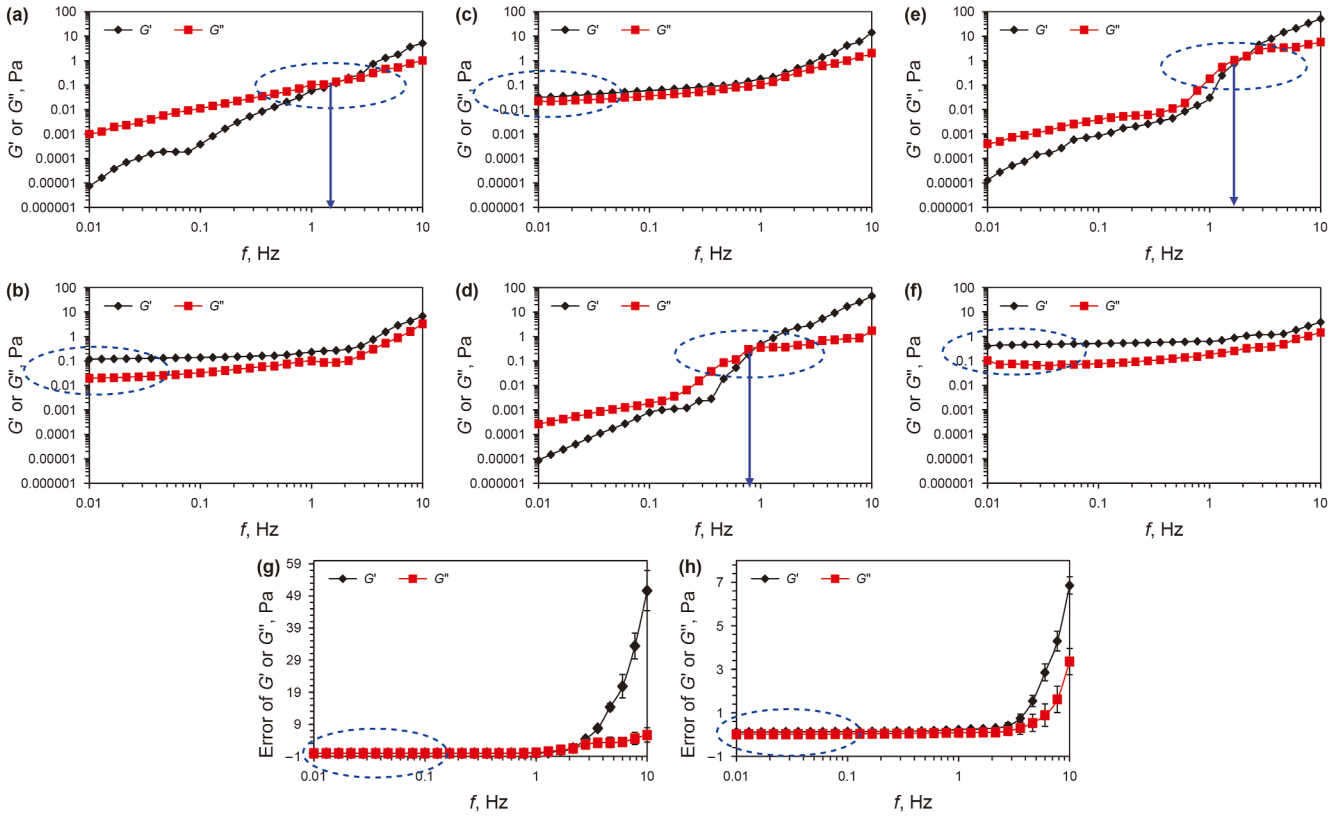

Fig. 6. Viscoelastic curve changes of different concentrations of CRS-10 system before and after assembly (at different temperatures). 0.075% CRS-10 before (**a**) and after (**b**) assembly, 25 °C; 0.20% CRS-10 before (**c**) and after (**d**) assembly, 25 °C; 0.20% CRS-10 before (**e**) and after (**f**) assembly, 70 °C. (**g**, **h**) Error displays of (c) and (d), respectively.

results show that before assembly, with the increase in the concentration of CRS-10 friction reducer, the intersection point of the viscoelastic modulus curve gradually moves to the left, showing that the elastic region begins to appear (as shown in Fig. 6(a, c)). After assembly, regardless of the polymer concentration, the elastic modulus (G') of the fluid system is always greater than the viscous modulus (G''), indicating that the assembled fluid has high elastic properties. Specifically, the elastic modulus at zero shear rate (0.01 Hz) increases by 4420.18 times after 0.075% CRS-10 polymer is assembled with nano-emulsion. When the polymer concentration is increased to 0.20% and assembled, the elastic modulus is increased by an order of magnitude, reaching 9376.97 times. In addition, when the polymer concentration of the CRS-10 assembled fluid system increases from 0.075% to 0.20%, the elastic modulus at 0.01 Hz increases by 3.65 times, while the viscous modulus changes little (as shown in Fig. 6(b, d)). In the case of similar viscosity, the elastic modulus of 0.075% assembled fluid is about 2570.19 times higher than that of 0.20% before assembly at 0.01 Hz, while the viscous modulus only increases by 55.88 times (as shown in Fig. 6(b, c)). Under the heating condition, the elastic enhancement of the fluid is more significant, and the elastic modulus at 0.01 Hz is further improved. In contrast, if the elastic effect is ignored, the viscous sand-carrying capacity of the conventional friction reducer before assembly decays faster (as shown in Fig. 6(e, f)). This indicates that the increase in temperature is beneficial to the enhancement of fluid elasticity, thus promoting the assembly effect. It is speculated that this is due to the increase in ionization degree or the thinning of hydration layer caused by the increase in temperature, which makes the interaction between anion and cation stronger. Under near-zero/low shear-rate conditions, three replicates of the viscoelastic modulus are obtained, with very small standard deviations, as low as 0.000178 (as shown in Fig. 6(g, h)). Measurement variability increases only at higher shear frequencies, therefore the order-of-magnitude increase in elastic modulus at near-zero shear is reliable. Note that a logarithmic *y*-axis can mask negative error. To clearly show the very small deviations, log scaling is removed and only the two rheology curves before and after assembly (where the modulus changes by orders of magnitude) are presented to emphasize the difference.

3.2. Sand-carrying capacity

3.2.1. Room temperature static sand-carrying capacity of CRS-10 fluid system

Four different kinds of 0.05% anionic surfactants are selected to assemble with CRS-10, and their static sand-carrying effects at room temperature are compared, the sand-carrying experiment is supplemented when the polymer concentration is reduced. The experimental results show that the four anionic nano-emulsion systems have almost no sand settlement in the first 5 min (as shown in Fig. 7(b)). But at 15 min, the AES system begins to show an obvious settling phenomenon. At 30 min, most of the sand in the AES and AOS fluid systems has settled. After 1 h, the settling process is completed (as shown in Fig. 7(c–e)). In contrast, the fluid system assembled by SDBS and CRS-10 has not seen sand settlement even after 5 h (as shown in Fig. 7(f)). It is worth noting that even if the concentration of CRS-10 friction reducer is reduced, the assembled fluid system still exhibits effective sand-carrying capacity. The above sand-carrying phenomenon is highly consistent with the change trend of fluid viscosity after assembly.

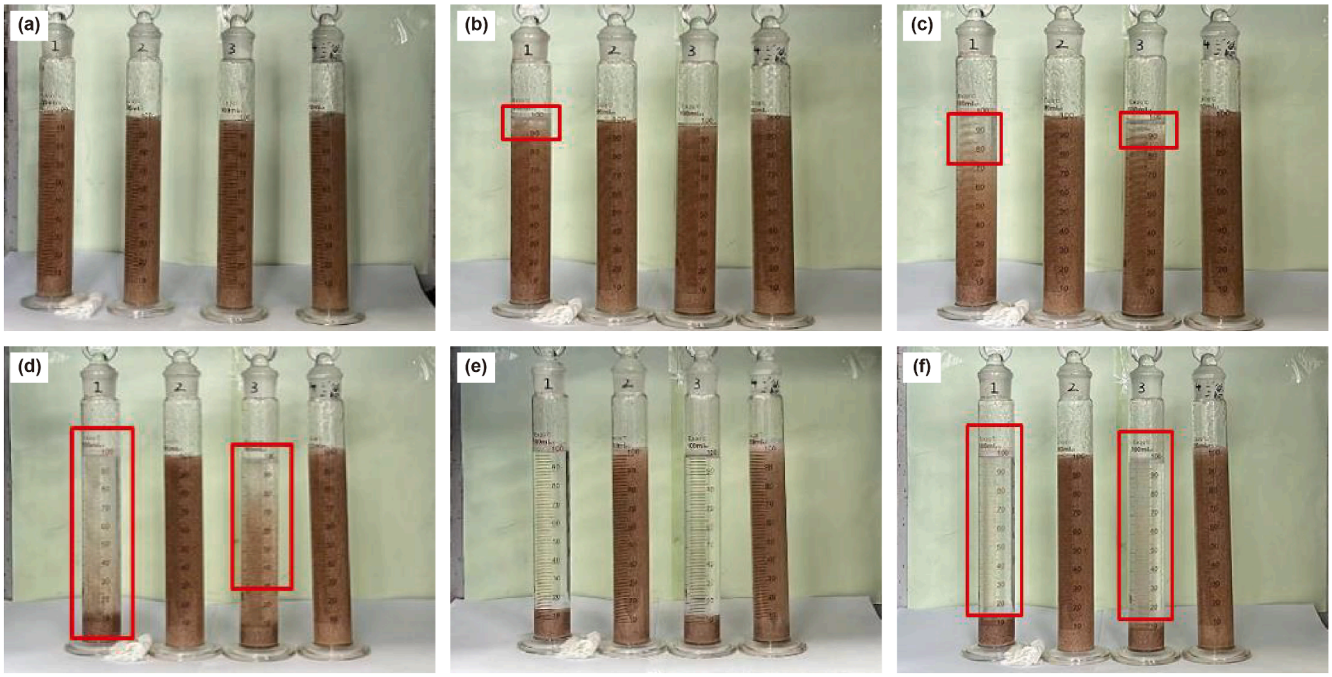

Fig. 7. Room temperature static sand-carrying capacity after assembly of different nano-emulsions and CRS-10 friction reducer. Formulation shown (from left to right): AES + 0.20% CRS-10, SDBS + 0.20% CRS-10, AOS-1 + 0.20% CRS-10, SDBS + 0.15% CRS-10). Images captured at 0 min (**a**), 5 min (**b**), 15 min (**c**), 30 min (**d**), 1 h (**e**), 5 h (**f**).

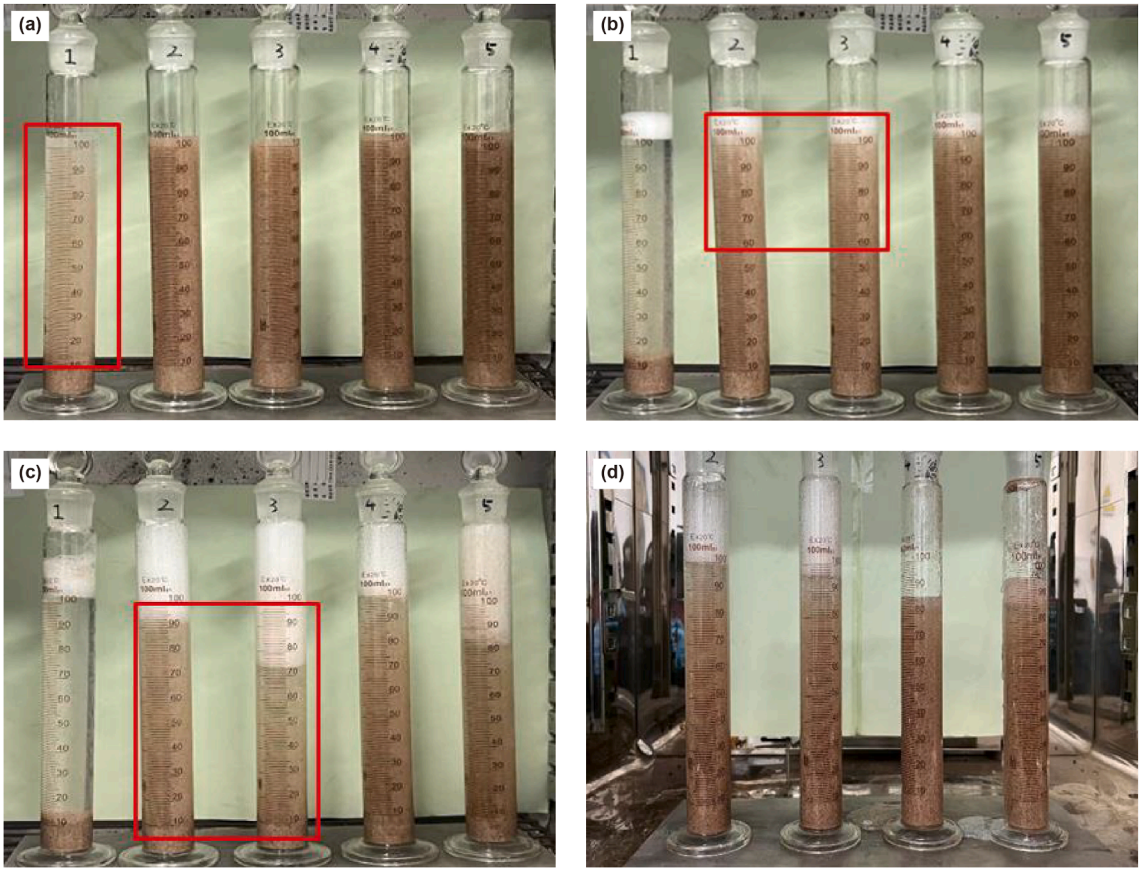

Fig. 8. High-temperature static sand-carrying condition after assembly of 0.05% SDBS and different concentrations of CRS-10 friction reducer. CRS-10 concentration from left to right: 0.075%-only one measuring cylinder, 0.15% and 0.20% each two. Images captured at 70 °C (**a**), 100 °C (**b**), 120 °C (**c**), and 130 °C (**d**).

3.2.2. High-temperature static sand-carrying capacity of CRS-10 fluid system

Only the sand-carrying effect of CRS-10 fluid at room temperature is explored, which is quite different from the performance at field reservoir temperature. Therefore, the high-temperature static sand-carrying test of CRS-10 assembled fluid system with different concentrations at different simulated reservoir temperatures is carried out, and the test time at each temperature is 2 h. The test process is to continue to heat up, keep the constant temperature for 30 min after heating up, and then observe the sand-carrying situation. As shown in Fig. 8(a), at 70 °C, the low concentration (0.075%) CRS-10 system has sand settlement, but the low viscosity fluid can still carry some sand at the reservoir temperature and not completely settle down. For 0.15% and 0.20% CRS-10 fluid systems, there is almost no significant settlement until the temperature rises to 100 °C (as shown in Fig. 8(b)). At this time, the sand in the low-viscosity fluid completely settles, and the settling time is more than 5 min, which is much longer than the low-viscosity fluid used in the field. At the same time, a small amount of sand settlement occurs in the 0.15% concentration system, and the settlement is more obvious at 120 °C (as shown in Fig. 8(c)). Considering that the fluid is not taken out and shaken well in the whole heating stage, the sand-carrying experiments of medium and high viscosity fluid after shaking well at 130 °C are further supplemented. The results show that it can still maintain good high-temperature elastic sand-carrying performance (as shown in Fig. 8(d)).

3.2.3. Dynamic sand-carrying capacity of CRS-10 fluid system

The static sand-carrying test at different temperatures shows that the CRS-10 assembled fluid system has a strong sand-carrying capacity. However, to be closer to the practical application, it is necessary to further investigate the sand-carrying effect of the fluid in the fracture flow state. To this end, different proportions of proppant (40/70 mesh quartz sand, sand ratio range of 10% to 30%) are added to the fluid, and the mixed sand-carrying fluid is injected into the visual fracture model through the pumping device and hose.

As shown in Fig. 9(a), the CRS-10 fluid before assembly has a large amount of sand settlement at 10% sand ratio, especially in the middle of the fracture model, indicating that the fluid is difficult to carry the sand to the end of the fracture. Under the condition of low sand ratio, the sand equilibrium bank height reaches 15 cm, accounting for half of the fracture height. When the sand ratio is further increased to 30%, the sand generates a large amount of settlement at the front end of the fracture and causes the pipeline to be blocked, the fluid cannot flow, and the sand bank becomes flat.

As shown in Fig. 9(b), under the same polymer concentration, the CRS-10 fluid after assembly can still carry more than 30% of the proppant even at a lower displacement (20 L/min). Because the injection direction is from top to bottom, the sand settlement mainly occurs at the back end of the fracture. In the dynamic sand-carrying test, when the sand ratio is 10%, the sand equilibrium bank height stabilizes at 6 cm. Increasing the sand ratio to 30% raises the sand equilibrium bank height to 9 cm, which is only about 30% of the total fracture height, indicating a limited increase.

Sand-carrying tests of the field standard fracturing fluid are added under identical experimental conditions for comparison (as shown in Fig. 9(c)). When its viscosity is matched to the CRS-10 assembly system and the sand ratio is 10%, the standard fluid carries sands better than the pre-assembly CRS-10 fluid but is slightly inferior to the CRS-10 assembly system. As the sand ratio increases, the sand bank in the fracture becomes markedly higher and more uneven, with sand equilibrium bank height exceeding half the fracture model, indicating that at comparable viscosities the standard field fluid still underperforms the CRS-10 assembly system.

Overall, these results indicate that the elasticity of the CRS-10 fluid stabilizes its proppant transport under dynamic flow, and the dynamic sand-carrying performance correlates well with the rheological behavior and static sand-carrying capacity.

Fig. 9. Comparison of dynamic sand-carrying before and after CRS-10 assembly (different sand ratios). (**a**) Before the assembly of CRS-10 system; (**b**) after the assembly of CRS-10 system; (**c**) field-standard fracturing fluids.

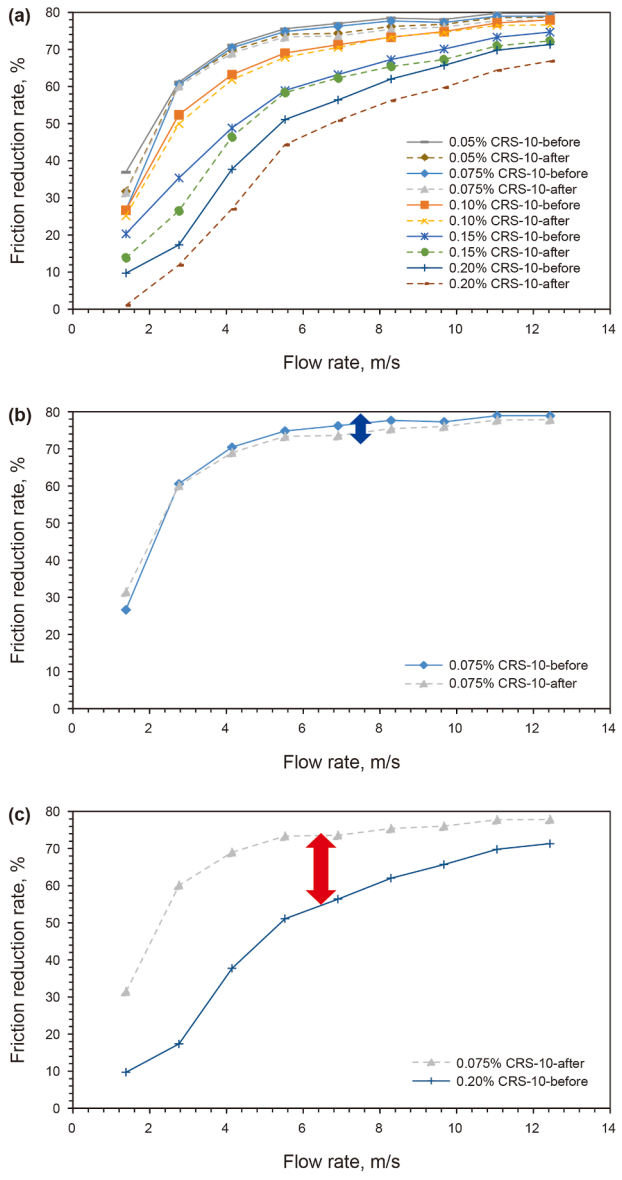

Fig. 10. Changes in friction reduction rate and viscoelastic contribution of CRS-10 fluid system. (**a**) Friction reduction rate of CRS-10 fluid system before and after assembly; (**b**) friction reduction rate difference of friction reducers with the same concentration; (**c**) friction reduction rate difference of friction reducers with the same viscosity.

3.3. Friction reduction performance

As shown in Fig. 10(a), CRS-10 fluid system shows a significant friction reduction effect. The friction reduction rate tends to be stable at higher flow rates, and the friction reduction rates before assembly remain above 70%. It is worth noting that the friction reduction performance of the CRS-10 fluid system decreases after the addition of nano-emulsion.

Under the same polymer concentration (0.075%), the fluid friction reduction rate before and after assembly does not change much (as shown in Fig. 10(b)), the viscosity increases slightly, but the elasticity increases significantly. Comparing two fluids with similar viscosity (0.20% before assembly and 0.075% after assembly), the test results show that the friction reduction rate of the fluid after low concentration assembly is significantly higher than that before high concentration assembly, and the difference is significant (as shown in Fig. 10(c)). This shows that the friction reduction effect of the polymer mainly depends on the entanglement state between the polymer molecules, and there is no necessary connection between the friction reduction rate and the viscosity. When the polymer concentration is large, it is difficult to form a good linear structure during the shearing and stretching process, resulting in a decrease in the ability to suppress turbulence. Therefore, increasing elasticity by reducing the polymer concentration is an effective way to improve the friction reduction rate (Bichler et al., 2021; Saeed and Elbing, 2023; Patel et al., 2023).

The fluid before assembly conforms to the friction reduction model of the traditional friction reducer. The model obtains the rheological (viscoelastic) index n and the comprehensive parameter ξ by fitting the Reynolds number (Re) and the friction coefficient. The relevant formulas are shown in Eqs. (2)–(4) (Bai et al., 2021). Specifically, $n = 1.932$, $\xi = 2.782$ for 0.20% CRS-10 fluid before assembly (as shown in Fig. 11(a)). After assembly, the overall trend of the friction reduction rate model does not change, indicating that the elastic enhancement does not alter the change rule of the fluid friction reduction rate, but changes the rheological index n and the comprehensive parameter ξ. For example, $n = 1.69$, $\xi = 8.37$ (as shown in Fig. 11(b)) of the 0.20% assembled fluid, indicates that the increase in elasticity leads to significant changes in parameters, thereby optimizing friction reduction performance.

$$Re = \frac{4Q\rho}{\pi D\mu} \tag{2}$$

$$f = 0.25\lambda = \frac{\pi\Delta PD^5}{128\rho LQ} \tag{3}$$

$$f^{-\frac{1}{2}} = \frac{4}{n^{0.75}}\lg\left[Re \times f^{\left(1-\frac{n}{2}\right)}\right] - \frac{0.4}{n^{1.2}} - 2.1\xi \tag{4}$$

3.4. Gel breaking and imbibition performance

The gel-breaking test of the supramolecular assembly fracturing fluid system is carried out at different simulated reservoir temperatures by using 400 mg/L ammonium persulfate. The results show that the assembled fluid system after gel breaking is clear and transparent, and there is no visible residue after centrifugation. Under low temperature conditions, although the gel breaking time is prolonged, the gel breaking is more thorough, and the overall residue content is less than 50 mg/L (as shown in Fig. 12(a)).

Subsequently, the imbibition experiment of saturated oil core is carried out at the reservoir temperature (70 °C). The results of NMR T_2 test show that the fluid system can synergistically mobilize crude oil with different pore sizes in tight sandstone. The oil mobilization rate in micron-sized large pores and nano-sized small pores exceeds 40%, and the overall oil recovery rate reaches 42.70% (as shown in Fig. 12(b, c)). This is mainly due to the small particle size, low adsorption, and strong wetting modification of nano-emulsion (as shown in Fig. 12(d)), and the addition of polymer CRS-10 further promotes the oil mobilization efficiency.

4. Mechanism validation

4.1. Changes of ^{1}H NMR spectrum before and after CRS-10 assembly

The ^{1}H NMR tests of CRS-10 single agent, SDBS nano-emulsion, and the assembled fluid system by them are carried out with an

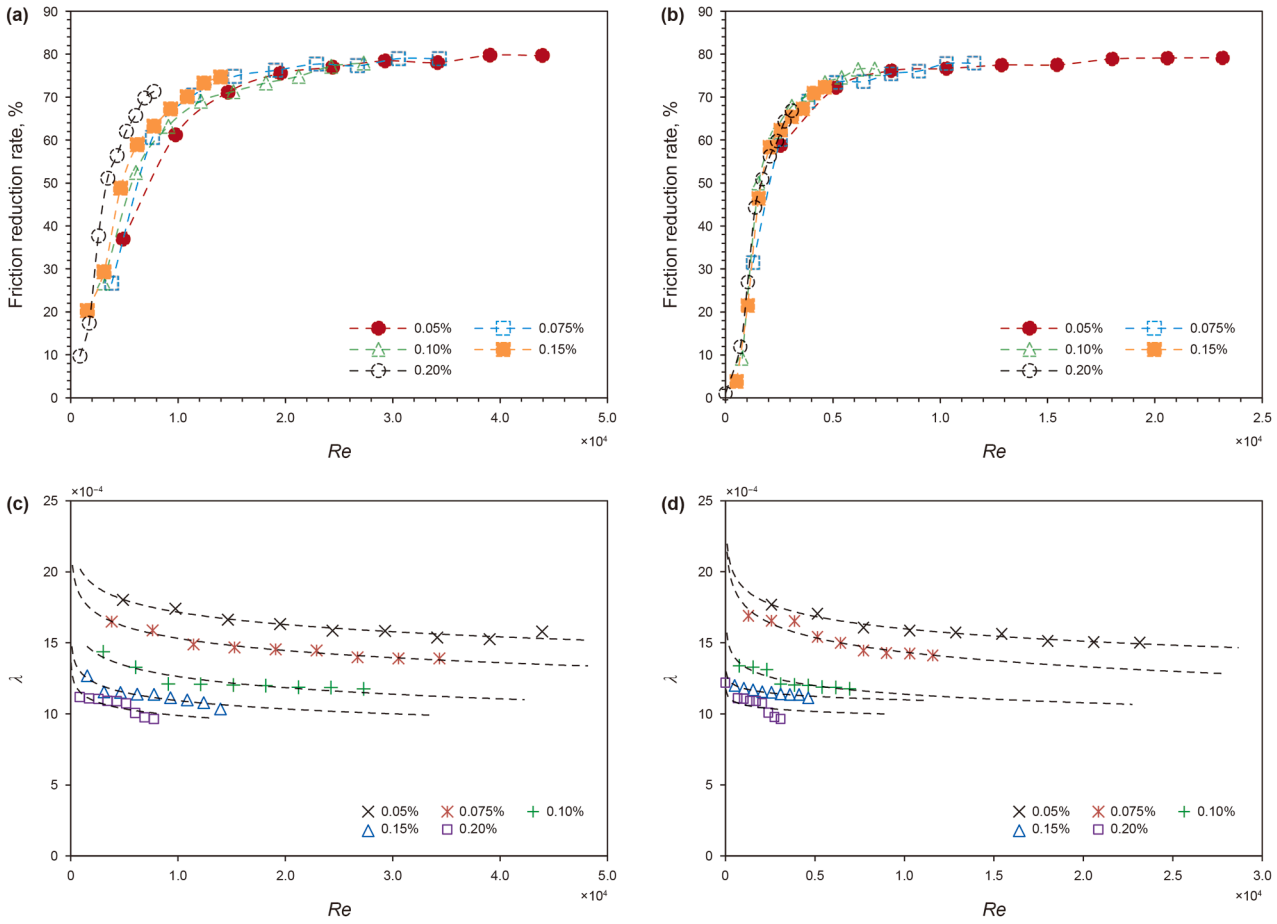

Fig. 11. The friction reduction rate model fitting of CRS-10 fluid system before and after assembly. Reynolds number and friction reduction rate relationship before (**a**) and after (**b**) assembly; friction reduction model fitting before (**c**) and after (**d**) assembly.

NMR spectrometer after low-temperature drying. The main principle is that by studying the absorption of radio-frequency radiation by atomic nuclei, the composition and molecular structure of organic and inorganic substances can be efficiently and qualitatively analyzed.

The ^{1}H NMR spectrum of the three systems are superimposed and corrected by the 4.9 ppm peak corresponding to the heavy water (D_2O) to align the absorption peaks. Subsequently, the difference in the absorption peaks of the ^{1}H NMR spectrum of the CRS-10 single agent and the assembled fluid system is amplified and compared, and the change in the chemical shift is combined to determine whether there is a significant interaction.

As shown in Fig. 13, a significant left shift of the chemical shift (in the direction of the high field) is observed at 3.72 ppm. Combined with molecular structure analysis, the peak corresponds to the methyl group ($–CH_3$) in the polymer cationic monomer DMAAC18. The left shift phenomenon indicates that the sulfonate group ($–SO_3^-$) in the SDBS nano-emulsion and the quaternary ammonium salt cation ($–N^+(CH_3)_2–$) in the CRS-10 polymer are ionized and assembled to form a tight ion pair. The negative charge part neutralizes the positive charge, reducing the de-shielding effect on the adjacent methyl group, causing the chemical shift to move toward the high field direction (Colherinhas et al., 2019; Goudie et al., 2023; Zhang et al., 2018).

4.2. Structure of CRS-10 fluid system by transmission electron microscopy

The CRS-10 fluid systems before and after assembly at different concentrations are observed by transmission electron microscopy (TEM, Quanta200 type). The results show that the pure polymer solution of 0.05% CRS-10 shows a network structure, but it only shows a two-dimensional network structure without adding nano-emulsion before assembly, with fewer assembly sites, and the average wall thickness of the polymer is only 5.58 μm (as shown in Fig. 14(a)). The structural strength and viscoelasticity of the CRS-10 fluid system is weak, and it is difficult to achieve effective sand carrying. After the addition of nano-emulsion, the CRS-10 fluid system forms a three-dimensional assembly structure. As the polymer concentration of CRS-10 gradually increases from 0.05% to 0.10%, the density of the polymer network increases significantly, and the fluid system finally shows solid-like characteristics. When the concentration is further increased to 0.20%,

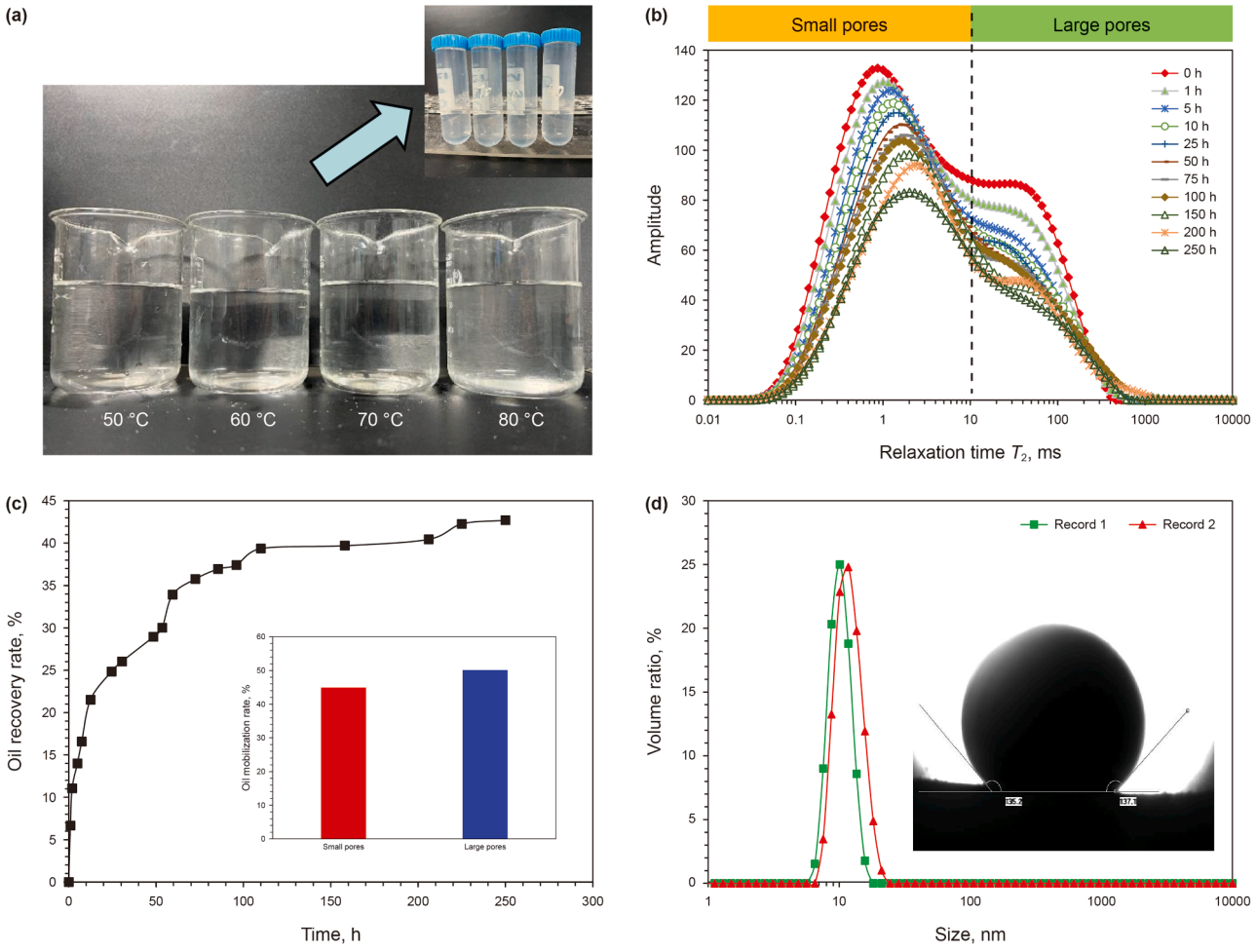

Fig. 12. Analysis of gel breaking, imbibition, and fluid properties of CRS-10 system after assembly. (**a**) Gel breaking situation at different temperatures; (**b**) imbibition situation of gel-breaking fluid; (**c**) total oil recovery rate and oil mobilization rate for different pore sizes; (**d**) particle size and modification degree of gel-breaking fluid system.

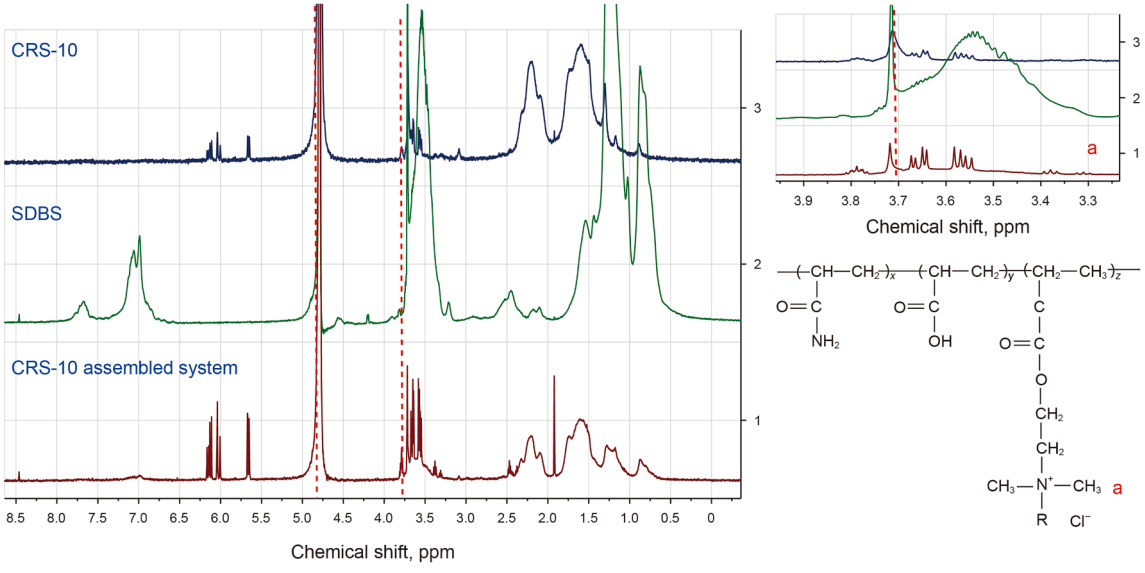

Fig. 13. Molecular structure changes of CRS-10 single-agent and assembled fluid system.

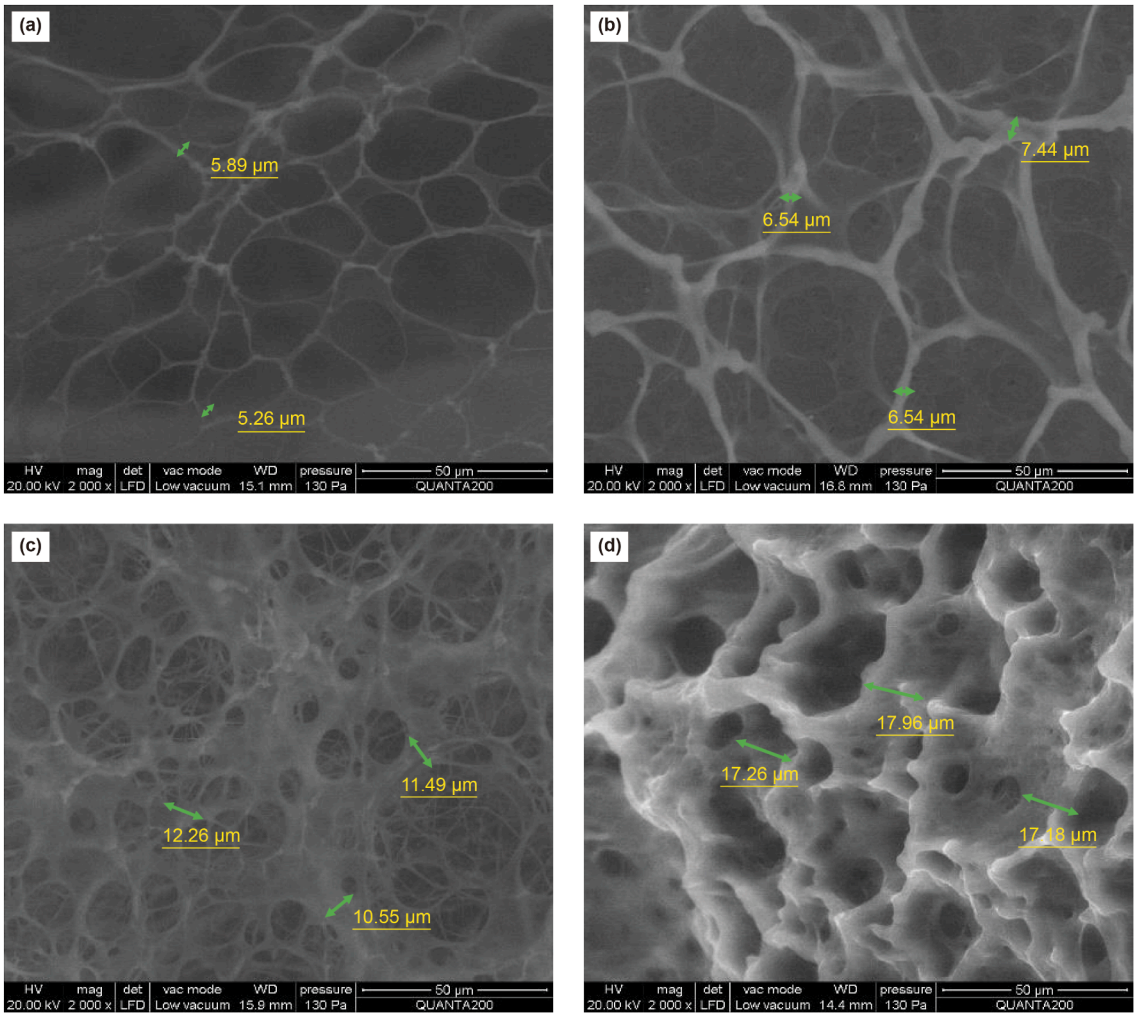

Fig. 14. TEM images of CRS-10 fluid system before and after assembly. 0.05% CRS-10 before (**a**) and after (**b**) assembly; 0.10% (**c**) and 0.20% (**d**) CRS-10 after assembly.

the polymer wall thickness increases significantly from 6.54 to 17.96 μm (as shown in Fig. 14(b–d)). The above results show that the assembly promotes the three-dimensional physical cross-linking of the polymer network, significantly improves the structural strength and viscoelastic properties of the fluid, thereby enhancing its sand-carrying capacity and friction reduction stability.

Compared with the network structure of conventional polymer fracturing fluids, the CRS-10 assembly system exhibits a denser and stronger mesh-like network that behaves in a quasi-solid manner. Unlike VES fracturing fluids, the CRS system forms this network with only a small polymer dosage, and the network wall thickness is substantially increased (Liu et al., 2023; Xu Y. et al., 2023; Zhang W. et al., 2020)

4.3. Conductivity test and adsorption rate calculation of CRS-10 fluid system

The change of conductivity not only reflects the change of ion concentration in the solution, but also reveals the degree of interaction between CRS-10 polymer chain and SDBS nano-emulsion. When the two form a strong assembly, the polymer becomes part of the assembly complex, limiting the movement of free ions, thereby reducing the conductivity.

As shown in Fig. 15(a), with the increase in SDBS nano-emulsion or polymer CRS-10 concentration, the conductivity shows a gradual upward trend. This is because the increase in surface active substances increases the degree of freedom of ions and enhances the conductivity. By comparing the difference in the conductivity of the fluid system before and after the assembly, combined with Eq. (5) (Dukhin and Parlia, 2018; Zhang H. et al., 2020), the concentration change corresponding to the pure nano-emulsion is obtained, which is used to characterize the change in the adsorption rate. The results show that with the increase in nano-emulsion concentration, the adsorption rate gradually increases, and tends to be saturated in the concentration range of 0.05% to 0.10%, close to 100%.

As shown in Fig. 15(b), when the concentration of nano-emulsion is fixed at 0.05% and the concentration of polymer CRS-10 is lower than 0.20%, the adsorption rate of nano-emulsion increases with the increase in polymer dosage. However, when the polymer concentration exceeds 0.20%, polymer chains in the fluid system begin to self-assemble, and the assembly sites decrease, resulting in a decrease in the adsorption capacity of the surfactant in the nano-emulsion and a significant decrease in the adsorption rate.

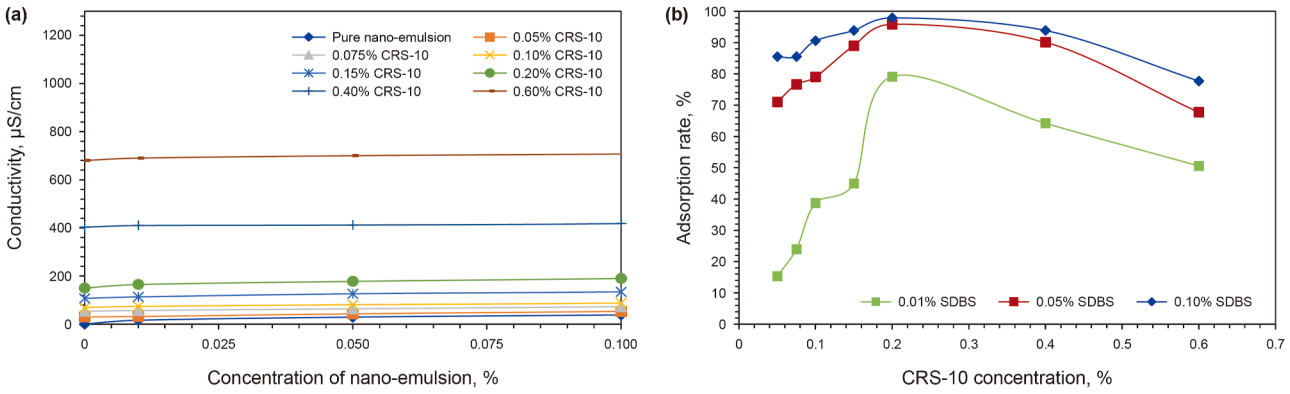

Fig. 15. Adsorption rate of surfactant in CRS-10 fluid varies with polymer concentration (conductivity method). (**a**) Conductivity; (**b**) adsorption rate.

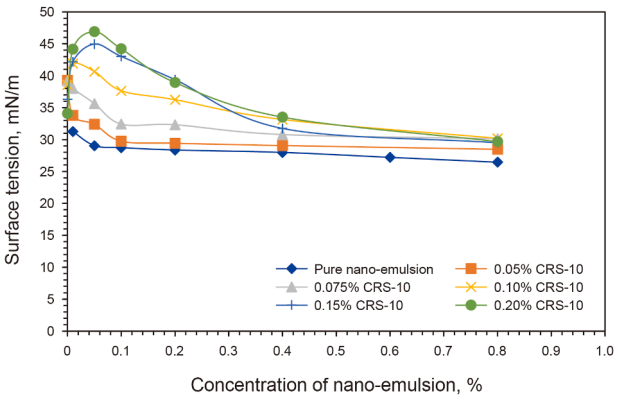

Fig. 16. Surface tension of CRS-10 fluid system varies with surfactant and polymer concentration (surface tension method).

$$\Gamma = \frac{C[D_{\text{CRS-10}} + D_{\text{SDBS}} - D_{\text{CRS}}]}{C_{\text{SDBS}}} \times 100\% \quad (5)$$

where Γ is adsorption rate, %; D is the conductivity, μS/cm; C is the reagent concentration, %.

4.4. Adsorption surface tension analysis and distribution diagram of CRS-10 fluid system

The change of surface tension is mainly affected by the adsorption of polymer and surfactant molecules at the solution interface, which can more intuitively reflect the interaction between the two. As shown in Fig. 16, the fluid surface tension generally decreases with the increase in the concentration of the polymer or nano-emulsion, which is due to the large adsorption of the active components in the pure polymer or surfactant solution

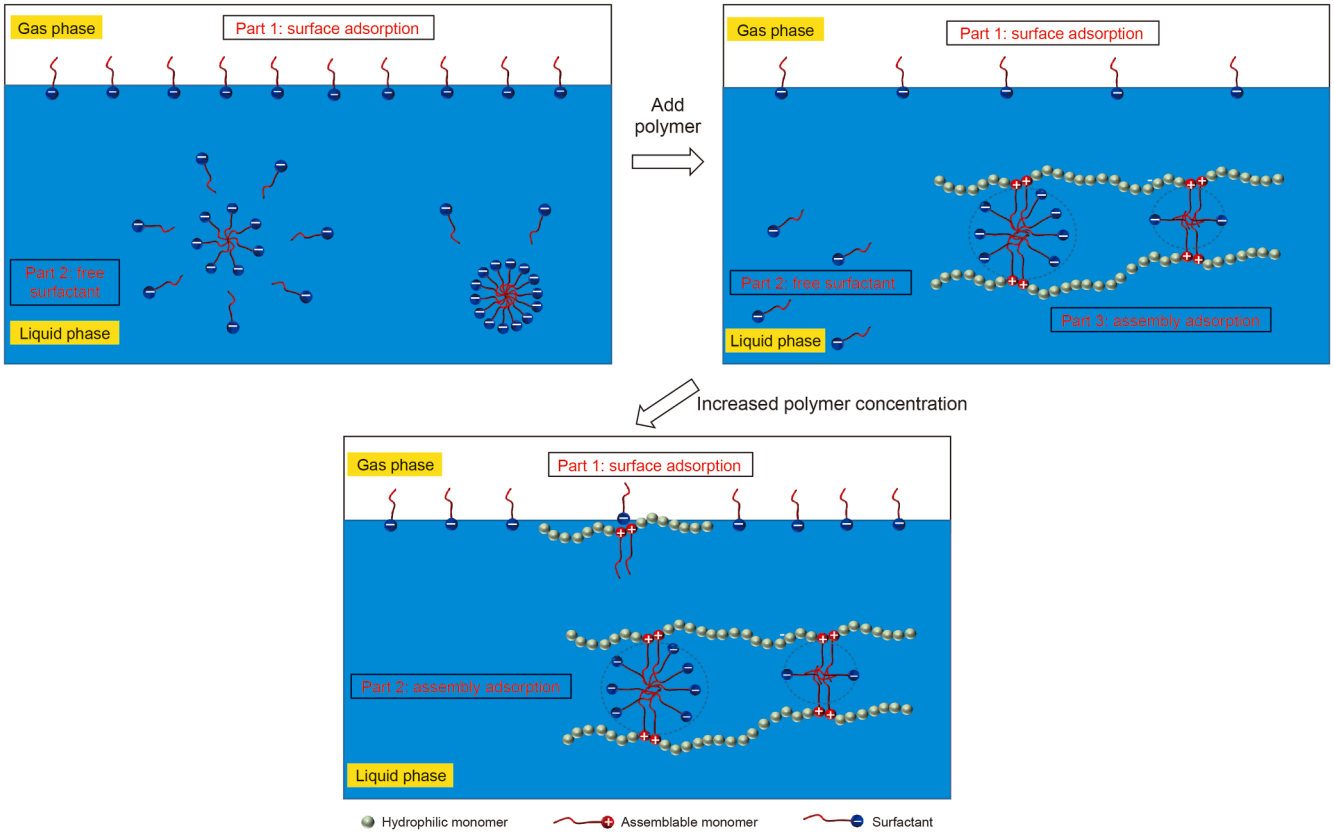

Fig. 17. Adsorption diagrams of surfactant and polymer at different stages.

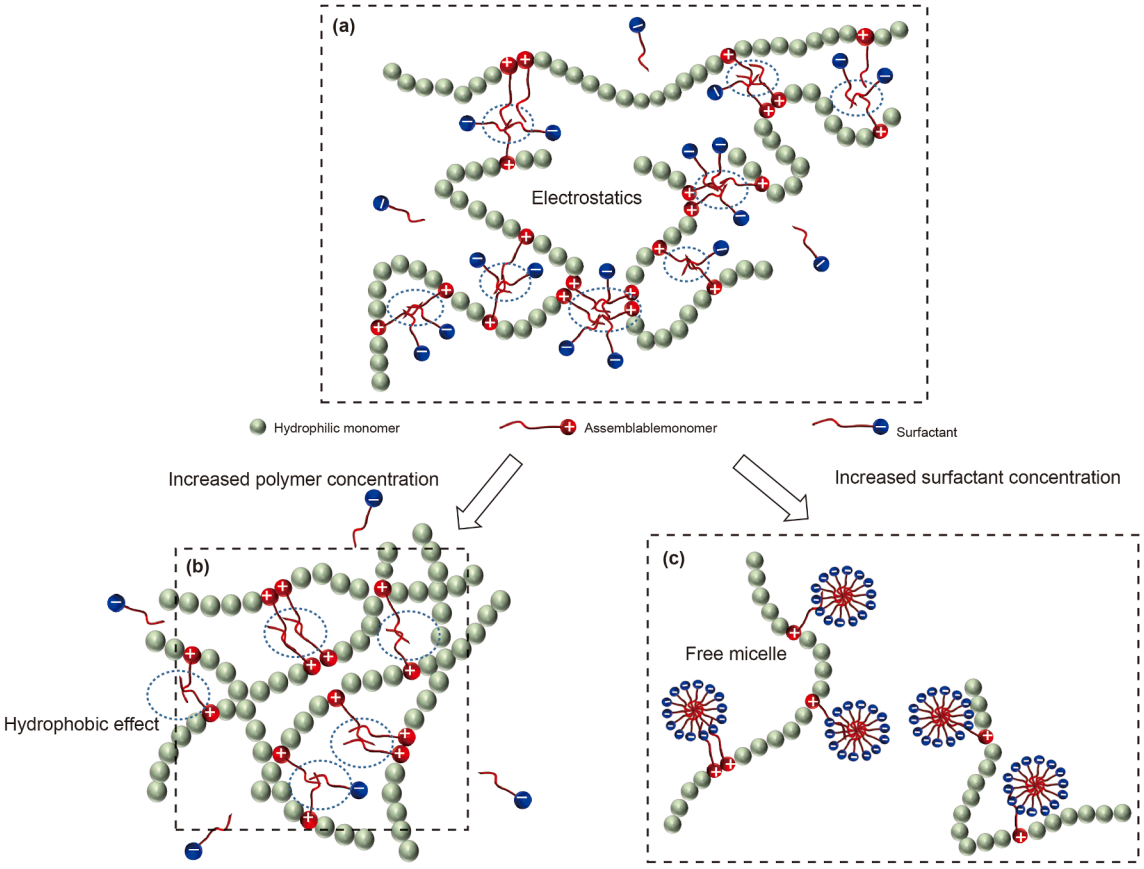

Fig. 18. Schematic diagrams of the assembly process of nano-emulsion and friction reducer polymer at different stages. (**a**) Adsorption and assembly phenomenon of polymer chains and surfactant; (**b**) assembly phenomenon when the polymer concentration increases; (**c**) assembly phenomenon when the surfactant concentration increases (forming free micelles).

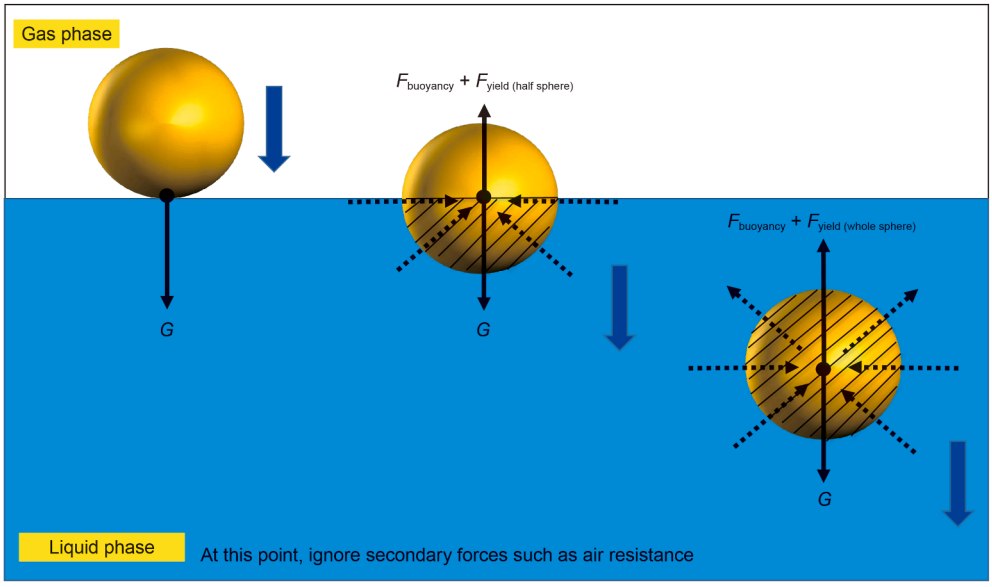

Fig. 19. Force changes of proppant particles in CRS-10 fluid system.

at the fluid interface. This phenomenon is similar to the changes in conductivity. When the concentration of nano-emulsion is fixed at 0.05%, the surface tension increases first and then decreases with the increase in polymer concentration. This is because the polymer concentration exceeds a certain threshold before it is assembled with the surfactant, resulting in some surfactant being absorbed onto the polymer chain, reducing the number of surfactant molecules that can be freely distributed to the interface. Specifically,

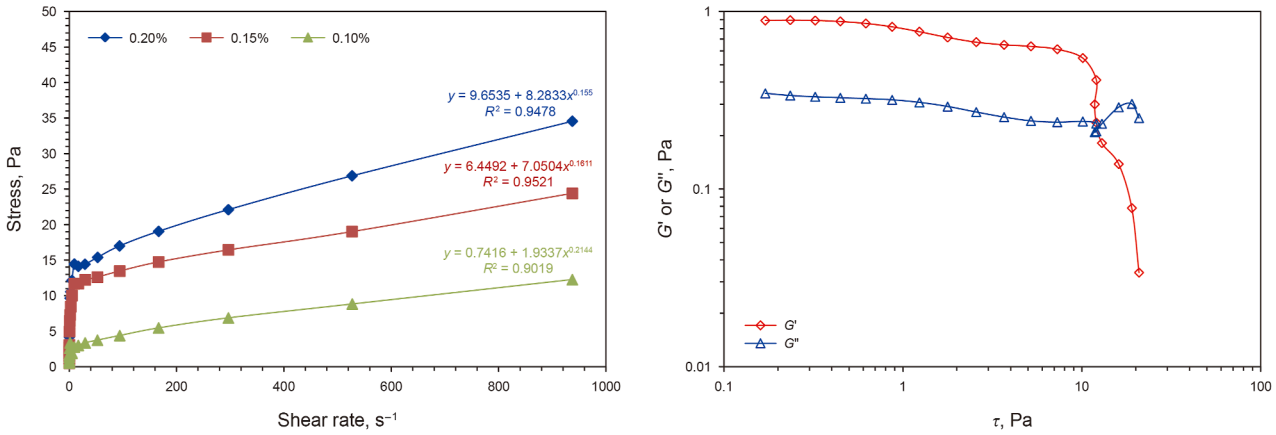

Fig. 20. Yield stress curves of different concentrations of CRS-10 fluid system after assembly.

the CRS-10 assembled fluid system with a concentration of 0.20% preferentially exists inside the liquid phase. As the CRS-10 system in the liquid phase gradually saturates, the assembled fluid system gradually migrates to the surface of the solution, so that the surfactant and polymer molecules coexist on the surface of the solution. The dispersed adsorption state of the above surfactant and polymer is shown in Fig. 17, which intuitively shows the interaction characteristics of the two at the interface.

4.5. Electrostatic attraction in CRS-10 fluid system

As shown in Fig. 18(a), the CRS-10 polymer has a positively charged functional group, while the surfactant in the SDBS nano-emulsion has a negative charge. The two are attracted by electrostatic interaction to form a low-viscosity and high-elastic fracturing fluid system that can be specifically identified and supramolecularly assembled. The positive charge group on the polymer chain is combined with the head of the negative charge of SDBS to form an orderly and uniform ionized adsorption layer, which promotes the good assembly of nano-emulsion and polymer. This process is helpful to improve the friction reduction stability and viscoelastic properties of CRS-10 fluid system.

As shown in Fig. 18(b), when the concentration of CRS-10 polymer increases, the hydrophobic groups between the polymer chains are associated to form local aggregation or association. This association reduces the number of positive potential assembly sites that can be adsorbed by the nano-emulsion, resulting in a decrease in the binding ability of the SDBS nano-emulsion to the polymer and a poor assembly effect. This phenomenon limits the uniform distribution and adsorption of nano-emulsions and affects the stability of the overall assembled structure.

As shown in Fig. 18(c), when the concentration of SDBS nano-emulsion increases, the surfactant molecules gradually self-assemble to form a micelle structure. The formation of micelles leads to the negative charge of the surfactant being coated inside the micelles or uniformly distributed, which makes it difficult to effectively electrostatically attract the positively charged groups of the polymer directly. This structural change hinders the effective assembly of nano-emulsions with polymers and reduces the assembly efficiency and stability of the system.

In summary, the assembly of polymer CRS-10 and SDBS nano-emulsion depends on electrostatic attraction, but the hydrophobic association caused by the increase of polymer and the micelles formed by the increase of nano-emulsion will affect the assembly site and adsorption effect, resulting in the decrease of assembly performance. Reasonable regulation of the concentration and ratio of polymer and nano-emulsion is crucial for achieving a stable and efficient supramolecular assembly system.

4.6. Sand-carrying force of CRS-10 fluid system

When the fluid carries sand in the fracture, due to the small shear rate, the actual working condition is often close to the low (or zero) shear rate state. Therefore, the rheological parameters measured at low shear rate are generally used to characterize the sand-carrying performance. Some scholars believe that the sand-carrying process at this time is similar to static sand carrying. The main forces include the yield stress of the fluid system, the buoyancy of the proppant and its gravity (referred to as net gravity) (Accetta and Venerus, 2024; Fraggedakis et al., 2016). The force relationship is shown in Fig. 19. Based on this, the yield stress of CRS assembled fluid system with different concentrations is tested using a rheometer. The results can be obtained by variable shear rate method and variable shear stress method.

As shown in Fig. 20, the yield stress of 0.20%, 0.15%, and 0.10% CRS-10 fluid systems at zero shear rate is 9.6535, 6.4492, and 0.7416 Pa, respectively. The 40/70 mesh quartz sand used in the experiment can be seen as a circular particle with a radius of about 0.16 mm. The net gravity (gravity-buoyancy) is $\frac{4}{3}\pi r^3(\rho_p - \rho_w)g = 3.46$ Pa. It can be seen that when the CRS-10 concentration is greater than 0.15%, the yield stress exceeds the net gravity, and CRS-10 fluid system can effectively support the proppant to prevent its settlement, reflecting the excellent sand-carrying performance. It is worth noting that this section is only based on a simplified mechanical analysis to explore the reasons for the good sand-carrying performance of the CRS-10 fluid system. The actual sand-carrying effect is also affected by many factors, which needs to be further studied in combination with more experiments and theoretical research.

5. Conclusions

This study developed an electrostatically assembled CRS-10 fracturing fluid that delivers low viscosity, high elasticity, high temperature and shear stability, and strong sand carrying, making it suitable for tight-reservoir fracturing.

(1) CRS-10 is synthesized by aqueous polymerization. Through supramolecular assembly, for instance electrostatic interactions between quaternary ammonium groups and

sulfonates, the polymer and SDBS nano-emulsions are assembled into a stable three-dimensional network.

(2) The assembled system exhibits low viscosity and high elasticity. Its zero-shear elastic modulus increased approximately 9377 times, and at equal viscosity, the modulus increased about 2570 times.

(3) The viscosity of the assembled system remains about 30 mPa·s at 120 °C and 170 s^{-1} even after prolonged shearing, and exceeds 800 mPa·s at low shear rates.

(4) Static sand-carrying tests shows no significant settling over 5 h. At a CRS-10 concentration of 0.20%, the yield stress reaches 9.65 Pa, far exceeding the net gravity of the 40/70 sand particles (3.46 Pa). At 30% sand ratio, the sand bank is about 30% of the fracture height, which is better than field-standard fracturing fluid.

(5) Friction reduction exceeds 70%. After gel breaking, the fluid becomes transparent with a residue concentration below 50 mg/L. The optimal formula (0.05%–0.20% CRS-10 + 0.05% SDBS) enhances oil recovery to 42.7%.

(6) NMR and TEM analyses confirm that electrostatic assembly forms network walls of approximately 17.96 μm, providing the system with its elastic properties. Conductivity and surface tension measurements reveal that higher polymer concentrations promote surfactant adsorption and supramolecular stability, thereby explaining the observed rheological behavior.

CRediT authorship contribution statement

Hao Bai: Writing – original draft, Formal analysis, Data curation. **Fu-Jian Zhou:** Resources, Funding acquisition, Conceptualization. **Zhi-Yuan Ding:** Formal analysis, Data curation. **Xin-Lei Liu:** Investigation, Formal analysis. **Sai Zhang:** Methodology, Investigation. **Kun Zhang:** Supervision, Methodology. **Wen-Jie Xie:** Validation, Supervision. **Yun-Jin Wang:** Visualization, Validation. **Rui-Jie Fei:** Formal analysis, Methodology. **Yue-Peng Dong:** Visualization, Validation. **Er-Dong Yao:** Writing – original draft, Funding acquisition, Conceptualization.

Declaration of competing interest

The authors declare that they have no known competing financial interests or personal relationships that could have appeared to influence the work reported in this paper.

Acknowledgements

This research was financially supported by the National Science and Technology Major Projects of China (Grant No. 2024ZD1404702) and the National Natural Science Foundation of China (Grant No. U25D9018).

References

Accetta, F., Venerus, D.C., 2024. The complex rheological behavior of a simple yield stress fluid. Rheol. Acta 63 (9), 719–730. https://doi.org/10.1007/s00397-024-01468-6.

Bai, H., Zhou, F.J., Zhang, M.C., et al., 2021. Optimization and friction reduction study of a new type of viscoelastic slickwater system. J. Mol. Liq. 344, 117876. https://doi.org/10.1016/j.molliq.2021.117876.

Bai, H., Zhou, F.J., Liu, X.L., et al., 2024. Study on pH-responsive delayed, cross-linking and weighted fracturing fluid. Molecules 29 (24), 5847. https://doi.org/10.3390/molecules29245847.

Bai, H., Wu, J.L., Zhou, F.J., et al., 2025. Mechanism research and field practice of elastic sand-carrying capacity in novel-functionality slickwater. Fuel 401, 135962. https://doi.org/10.1016/j.fuel.2025.135962.

Bichler, K.J., Jakobi, B., Schneider, G.J., 2021. Dynamical comparison of different polymer architectures—Bottlebrush vs linear polymer. Macromolecules 54 (4), 1829–1837. https://doi.org/10.1021/acs.macromol.0c02104.

Cai, J., Ma, X., Zhang, L., et al., 2023. Preparation of W/W suspension drag reducer and study on the properties of integrated slippery water. Colloids Surf. A Physicochem. Eng. Asp. 674, 131832. https://doi.org/10.1016/j.colsurfa.2023.131832.

Colherinhas, G., Oliveira, L.B.A., Castro, M.A., et al., 2019. On the calculation of magnetic properties of nucleic acids in liquid water with the sequential QM/MM method. J. Mol. Liq. 294, 111611. https://doi.org/10.1016/j.molliq.2019.111611.

Dukhin, A., Parlia, S., 2018. Adsorption of surfactant from non-polar liquid into porous material characterized using conductivity measurement. J. Colloid Interface Sci. 531, 523–532. https://doi.org/10.1016/j.jcis.2018.07.075.

Fraggedakis, D., Dimakopoulos, Y., Tsamopoulos, J., 2016. Yielding the yield-stress analysis: A study focused on the effects of elasticity on the settling of a single spherical particle in simple yield-stress fluids. Soft Matter 12 (24), 5378–5401. https://doi.org/10.1039/C6SM00480F.

Goudie, K.J., McCreath, S.J., Parkinson, J.A., et al., 2023. Investigation of the influence of pH on the properties and morphology of gelatin hydrogels. J. Polym. Sci. 61 (19), 2316–2332. https://doi.org/10.1002/pol.20230141.

Gusev, A.A., Schwarz, F., 2019. Molecular dynamics validation and applications of the maximum entropy homogenization procedure for predicting the elastic properties of Gaussian polymer networks. Macromolecules 52 (24), 9445–9455. https://doi.org/10.1021/acs.macromol.9b01766.

Han, X., Wu, J., Ji, Y., et al., 2024. Impact of viscoelasticity on sand-carrying ability of viscous slickwater and its sand-carrying threshold in hydraulic fractures. Energies 17 (2), 428. https://doi.org/10.3390/en17020428.

Hincapie, R.E., Borovina, A., Clemens, T., et al., 2022. Optimizing polymer costs and efficiency in alkali–polymer oilfield applications. Polymers 14 (24), 5508. https://doi.org/10.3390/polym14245508.

Hu, P., Wang, S., Yi, H., et al., 2024. Hybridized cellulose nanocrystals enhanced the temperature resistance and viscoelasticity of the fracturing fluid network. J. Mol. Liq. 399, 124269. https://doi.org/10.1016/j.molliq.2024.124269.

Hu, T., Zhao, Q., Wang, M., et al., 2023. Improved selectivity of molecularly imprinted polymers based on the synergistic action of hydrogen bond and electrostatic interaction. J. Mol. Recogn. 36 (7), e3024. https://doi.org/10.1002/jmr.3024.

Huang, G., Li, M., Zhou, F., et al., 2024. Visualization experiments and numerical simulation on the growth of fracture height in bedding-rich reservoirs. Phys. Fluids 36 (11), 117144. https://doi.org/10.1063/5.0242604.

Jin, C., Yi, N., Nie, C., et al., 2025. Study on the relationship between structure and performance of HPAM-based high viscosity friction reducer. Colloid Polym. Sci. 303 (3), 457–468. https://doi.org/10.1007/s00396-024-05361-9.

Keane, D.P., Kolozsvary, T., McDonald, B., et al., 2024. Bottlebrush midblocks promote colloidal bridging of telechelic polymers. ACS Macro Lett. 13 (10), 1304–1310. https://doi.org/10.1021/acsmacrolett.4c00428.

Lei, Q., Yang, Z., Weng, D., et al., 2022. Techniques for improving fracture-controlled stimulated reservoir volume in ultra-deep fractured tight reservoirs: A case study of Kuqa piedmont clastic reservoirs, Tarim Basin, NW China. Petrol. Explor. Dev. 49 (5), 1169–1184. https://doi.org/10.1016/s1876-3804(22)60341-0.

Liu, J., Liu, P., Du, J., Wang, Q., Chen, X., Zhao, L., 2023. Review on high-temperature-resistant viscoelastic surfactant fracturing fluids: State-of-the-art and perspectives. Energy Fuels 37, 9790–9821. https://doi.org/10.1021/acs.energyfuels.3c00488.

Liu, S., Zhao, M., Wu, Y., et al., 2022. Development and performance evaluation of a novel silica nanoparticle-reinforced CO_2-sensitive fracturing fluid with high temperature and shear resistance ability. Energy Fuels 36 (13), 7177–7185. https://doi.org/10.1021/acs.energyfuels.2c01056.

Liu, X., Zhang, X., Wen, Q., et al., 2020. Experimental research on the proppant transport behavior in nonviscous and viscous fluids. Energy Fuels 34 (12), 15969–15982. https://doi.org/10.1021/acs.energyfuels.0c02753.

Liu, X., Liu, Z., Bai, J., et al., 2025. Chain motion and energy variation of dynamic cross-linked polymers. Macromolecules 58 (11), 5842–5851. https://doi.org/10.1021/acs.macromol.5c00132.

Ma, X., Kong, S., Li, Z., et al., 2024. Effect of cross-linking density on the rheological behavior of ultra-soft chitosan microgels at the oil–water interface. J. Colloid Interface Sci. 672, 574–588. https://doi.org/10.1016/j.jcis.2024.06.026.

Mahata, S., Mondal, M.H., 2024. Study of polymer chain morphologies at and around critical concentrations. J. Polym. Res. 31, 344. https://doi.org/10.1007/s10965-024-04194-y.

Mao, J., Cao, H., Zhang, H., et al., 2022. Design of salt-responsive low-viscosity and high-elasticity hydrophobic association polymers and study of association structure changes under high-salt conditions. Colloids Surf. A Physicochem. Eng. Asp. 650, 129512. https://doi.org/10.1016/j.colsurfa.2022.129512.

Mohammadi, S., Afifi, H., Mahmoudi Alemi, F., 2024. Review on enhancing rheological characteristics of viscoelastic surfactant fracturing fluids by nanoparticles: Advances, challenges, and perspectives. Energy Fuels 38 (6), 4921–4945. https://doi.org/10.1021/acs.energyfuels.3c04977.

Othman, A., AlSulaimani, M., Aljawad, M.S., et al., 2022. The synergetic impact of anionic, cationic, and neutral polymers on ves rheology at high-temperature environment. Polymers 14 (6), 1145. https://doi.org/10.3390/polym14061145.

Patel, V., Trivedi, J., Sharma, T., 2023. Influence of hydrophobic association in the aqueous media on the rheology and polymer conformation of associative polymers. Polym. Bull. 80 (8), 8939–8959. https://doi.org/10.1007/s00289-022-04484-9.

Saeed, Z., Elbing, B.R., 2023. Polymer drag reduction: A review through the lens of coherent structures in wall-bounded turbulent flows. Phys. Fluids 35 (8), 081304. https://doi.org/10.1063/5.0162648.
Shi, S., Sun, J., Lv, K., et al., 2023. Preparation and performance evaluation of a variable viscosity friction reducer suspension with high salt tolerance and low damage. Energy Fuels 37 (2), 993–1005. https://doi.org/10.1021/acs.energyfuels.2c03494.
Wang, J., Zhou, F., Bai, H., et al., 2020. A new approach to study the friction-reduction characteristics of viscous/conventional slickwater in simulated pipelines and fractures. J. Nat. Gas Sci. Eng. 83, 103620. https://doi.org/10.1016/j.jngse.2020.103620.
Wang, J., Guo, P., Jiang, H., et al., 2022. A novel multifunction fracturing fluid compounding of nano-emulsion and viscous slickwater for unconventional gas and oil. Arab. J. Chem. 15 (5), 103749. https://doi.org/10.1016/j.arabjc.2022.103749.
Wang, Q., Zhou, F., Su, H., et al., 2024. Experimental evaluations of nano high-viscosity friction reducers to improve acid fracturing efficiency in low-permeability carbonate reservoirs. Chem. Eng. J. 483, 149358. https://doi.org/10.1016/j.cej.2024.149358.
Wang, T., Zhong, P., Li, G., et al., 2023. Transport pattern and placement characteristics of proppant in different rough fractures. Transport Porous Media 149 (1), 251–269. https://doi.org/10.1007/s11242-023-01965-x.
Wang, Y., Fu, J., Liu, M., Fu, Q., Zhang, J., 2019. Understanding the effect of chain entanglement state on melt crystallization of the polymer freeze-extracted from solution: The role of critical overlap concentration. Polymer 178, 121588. https://doi.org/10.1016/j.polymer.2019.121588.
Wen, J., Ming, Y., Zhang, A.F., et al., 2024. Interplay between hydrogen bond network and entangled network in polymers during stretching based on molecular simulations. Chin. J. Polym. Sci. 42 (12), 2069–2080. https://doi.org/10.1007/s10118-024-3227-0.
Xu, H., Li, Y., Yu, G.L., et al., 2023a. The enhancement of performance and imbibition effect of slickwater-based fracturing fluid by using MoS_2 nanosheets. Pet. Sci. 20 (4), 2187–2201. https://doi.org/10.1016/j.petsci.2022.12.008.
Xu, H., Zhou, F., Li, Y., Liu, C., Zhu, L., Yao, E., 2023b. Performance evaluation of oil-displacement viscoelastic zwitterionic surfactant fracturing fluid. J. Mol. Liq. 377, 121545. https://doi.org/10.1016/j.molliq.2023.121545.
Xu, H., Zhou, F., Wu, H., et al., 2024. Experimental research on the proppant settling and transport characteristics of silica gel-based fracturing fluid. SPE J. 29 (3), 1321–1336. https://doi.org/10.2118/218381-PA.
Xu, Y., Liu, K., Yang, Y., et al., 2023. Review. Hemicellulose-based hydrogels for advanced applications. Front. Bioeng. Biotechnol. 10, 1110004. https://doi.org/10.3389/fbioe.2022.1110004.
Xu, Z., Zhao, M., Liu, J., et al., 2024. Study on formation process and reservoir damage mechanism of blockages caused by polyacrylamide fracturing fluid in production wells. Fuel 358, 130154. https://doi.org/10.1016/j.fuel.2023.130154.
Yang, B., Zhao, J., Mao, J., et al., 2019. Review of friction reducers used in slickwater fracturing fluids for shale gas reservoirs. J. Nat. Gas Sci. Eng. 62, 302–313. https://doi.org/10.1016/j.jngse.2018.12.016.
Yang, F., Li, B., Wang, K., et al., 2024. Extreme massive hydraulic fracturing in deep coalbed methane horizontal wells: A case study of the Linxing Block, eastern Ordos Basin, NW China. Petrol. Explor. Dev. 51 (2), 440–452. https://doi.org/10.11698/PED.20230513.
Yang, Z., Zhao, M., Bi, W., et al., 2024. Synthesis and analysis of drag reduction performance of the temperature-resistant polymer slickwater for high temperature reservoirs. J. Mol. Liq. 397, 124137. https://doi.org/10.1016/j.molliq.2024.124137.
Yao, E., Bai, H., Zhou, F., et al., 2021. Performance evaluation of the multifunctional variable-viscosity slick water for fracturing in unconventional reservoirs. ACS Omega 6 (32), 20822–20832. https://doi.org/10.1021/acsomega.1c01986.
Yehia, F., Gado, W., Al-Gamal, A.G., et al., 2024. Synergistic effect of carbon nanotubes, zinc, and copper oxides on rheological properties of fracturing fluid: A Comparative Study. Processes 2 (3), 611. https://doi.org/10.3390/pr12030611.
Zang, Y., Wang, H., Wang, B., et al., 2024. Fracture propagation morphology and parameter optimization design of pre-CO_2 hybrid fracturing in shale oil reservoirs, Ordos Basin. Geoenergy Sci. Eng. 238, 212849. https://doi.org/10.1016/j.geoen.2024.212849.
Zarrin, N., Abbasi, M., Sadighi, M., et al., 2024. Energy dissipating of shear thickening gel reinforced with PVA polymer. Polym. Bull. 81 (13), 11893–11910. https://doi.org/10.1007/s00289-024-05264-3.
Zhang, H., Zhang, Y., Jia, Z., et al., 2020. Application of power law in conductivity of binary mixed rhamnolipid surfactant systems. Colloids Surf. A Physicochem. Eng. Asp. 603, 125190. https://doi.org/10.1016/j.colsurfa.2020.125190.
Zhang, K., Liu, Y., Sheng, L., et al., 2022. Study on the effect of fracturing fluid on the structure and mechanical properties of igneous rock. ACS Omega 7 (14), 11903–11913. https://doi.org/10.1021/acsomega.1c07386.
Zhang, L., Chai, X., Sun, P., et al., 2018. Characterization of the aggregated pattern of CHAPS using solvent paramagnetic relaxation enhancements. Colloids Surf. A Physicochem. Eng. Asp. 555, 332–338. https://doi.org/10.1016/j.colsurfa.2018.07.008.
Zhang, W., Mao, J., Yang, X., et al., 2020. Effect of propylene glycol substituted group on salt tolerance of a cationic viscoelastic surfactant and its application for brine-based clean fracturing fluid. Colloids Surf. A Physicochem. Eng. Asp. 584, 124043. https://doi.org/10.1016/j.colsurfa.2019.124043.
Zhang, Y., Qi, J., Wang, N., et al., 2024. Pseudo gemini surfactant fracturing fluid with dual function of fracturing and oil flooding for enhanced oil recovery. J. Mol. Liq. 393, 123562. https://doi.org/10.1016/j.molliq.2023.123562.
Zhao, M., Yan, X., Yan, R., et al., 2023. Synthesis and performance evaluation of water-in-water polymer drag-reducing agent. Colloids Surf. A Physicochem. Eng. Asp. 674, 131935. https://doi.org/10.1016/j.colsurfa.2023.131935.
Zhao, Z., Wang, M., Liu, T., et al., 2021. Effect and mechanism of rheological properties and structure of a novel hydrophobically associating polymer on sand sedimentation rate. J. Pet. Explor. Prod. Technol. 11 (7), 2943–2952. https://doi.org/10.1007/s13202-021-01208-z.
Zorgani, E., Al-Awadi, H., Yan, W., et al., 2018. Viscosity effects on sand flow regimes and transport velocity in horizontal pipelines. Exp. Therm. Fluid Sci. 92, 89–96. https://doi.org/10.1016/j.expthermflusci.2017.08.024.